BRNO UNIVERSITY OF TECHNOLOGY
VYSOKÉ UČENÍ TECHNICKÉ V BRNĚ

FACULTY OF MECHANICAL ENGINEERING
FAKULTA STROJNÍHO INŽENÝRSTVÍ

INSTITUTE OF PHYSICAL ENGINEERING
ÚSTAV FYZIKÁLNÍHO INŽENÝRSTVÍ

DEPTH PROFILING OF MULTILAYERS BY LEIS
HLOUBKOVÉ PROFILOVÁNÍ MULTIVRSTEV METODOU LEIS

MASTER'S THESIS
DIPLOMOVÁ PRÁCE

AUTHOR — **Bc. Tomáš Strapko**
AUTOR PRÁCE

SUPERVISOR — **Ing. Petr Bábor, Ph.D.**
VEDOUCÍ PRÁCE

BRNO 2019

VYSOKÉ UČENÍ TECHNICKÉ V BRNĚ
FAKULTA STROJNÍHO INŽENÝRSTVÍ

Zadání diplomové práce

Ústav:	Ústav fyzikálního inženýrství
Student:	**Bc. Tomáš Strapko**
Studijní program:	Aplikované vědy v inženýrství
Studijní obor:	Fyzikální inženýrství a nanotechnologie
Vedoucí práce:	**Ing. Petr Bábor, Ph.D.**
Akademický rok:	2018/19

Ředitel ústavu Vám v souladu se zákonem č.111/1998 o vysokých školách a se Studijním a zkušebním řádem VUT v Brně určuje následující téma diplomové práce:

Hloubkové profilování multivrstev metodou LEIS

Stručná charakteristika problematiky úkolu:

Nízkoenergiový rozptyl iontů (Low Energy Ion Scattering – LEIS) je často využíván při analýze čistoty povrchů a hloubkovém profilování tenkých vrstev. Pomocí energie rozptýleného iontu lze provést prvkovou analýzu studovaných povrchů. Pokud je povrch vzorku odprašován lze získat z měřených energiových spekter informaci o prvkové složení v závilosti na hloubce. Cílem diplomové práce je provést simulace energiových spekter pro metodu LEIS pro různé multivrstevnaté vzorky v modu hloukového profilování.

Cíle diplomové práce:

1. Proveďte simulace hloubkových profilů LEIS v programu TRBS pro různé vzorky.
2. Vyhodnoťe tyto simulace a porovnejte s experimentem.
3. Navrhňete optimální postup pro stanovení hloubkového profilu metodou LEIS

Seznam doporučené literatury:

FELDMAN, L. C., MAYER, J. W. Fundamentals of Surface and Thin Film Analysis, North Holland, New York 1986, 1-123.

RABALAIS, J. W. Low energy ion-surface interactions, John Wiley & Sons, New York 1994.

WOODRUFF, D. P., DELCHAR, T. A. Modern Techniques of Surface Science, Cambridge University Press 1986, 195-236.

Termín odevzdání diplomové práce je stanoven časovým plánem akademického roku 2018/19

V Brně, dne

L. S.

prof. RNDr. Tomáš Šikola, CSc. ředitel ústavu	doc. Ing. Jaroslav Katolický, Ph.D. děkan fakulty

Abstrakt

Diplomová práce se zabývá vytvořením modelu, který by umožnil lepší interpretaci hloubkových profilů měřených metodou LEIS. Obtížnost interpretace těchto profilů je dána vysokým podílem vícenásobně odražených projektilů v měřených spektrech. Tyto projektily nepřináší užitečnou informaci z dané hloubky. Naproti tomu jednonásobně odražené projektily nesou přesnější informaci o složení a tloušťce vrstev. V této práci vytvořený model se snaží určit příspěvek jednonásobně odražených částic k celkovému tvaru spektra a na základě něj i hloubkový profil vzorku.

Abstract

The master's thesis deals with introducing the model which would enable better interpretation of the depth profiles obtained by the LEIS method. The difficulty of the interpretation is caused by the significant contribution of multiple-scattered projectiles to the resulting measured spectra. These projectiles do not provide useful information from respected depth. In contrary, single-scattered projectiles yield more precise information about the composition and the thickness of the layers. The model created in the presented work attempts to determine the contribution of single-scattered particles to the resulting spectral shape and, based on the computation, a depth profile of the sample as well.

Klíčová slova

Nízkoenergiový iontový rozptyl, LEIS, model jednonásobního odrazu, TRBS

Keywords

Low Energy Ion Scattering, LEIS, single-scattering model, TRBS

STRAPKO, Tomáš. Depth profiling of multilayers by LEIS: Master's Thesis. Brno: Brno University of Technology, Faculty of Mechanical Engineering, Institute of Physical Engineering, 2019. 43 p. Supervised by Ing. Petr Bábor, Ph.D.

I declare that I wrote my master's thesis *Depth profiling of multilayers by LEIS* on my own, under the supervision of Ing. Petr Bábor, Ph.D., using the literature stated in bibliography.

Tomáš Strapko

I would like to thank my supervisor Ing. Petr Bábor, Ph.D. for his time, encouragement in the times of need and ever-lasting optimism despite the menacing approaching of a deadline in connection with my struggling to provide at least some sensible results.

I also thank Katarína Mokránová for her corrections of the grammar and general meaning alike, which is essential for ensuring the proper impression of the thesis.

I thank Radek Holeňák as well, for his positive and supporting attitude during our discussion of presented topics.

The gratitude for introducing me into the utilization of simulations and a deeper understanding of scattering specifics belongs to Barbara Bruckner and Daniel Primetzhofer from Ion Physics Group in Uppsala University, Sweden.

Finally, I would like to thank my parents, who always supported me in every regard and without whom this thesis would never be written.

Tomáš Strapko

Contents

Introduction

Low-Energy Ion Scattering (LEIS) is an extremely surface sensitive, non-destructive experimental method for the analysis of the ultra-thin layers. In classical LEIS experiment, ionized atoms of noble gasses with primary energies up to 10 keV are impinging on the studied material and are collected by a detector after a scattering under the desired angle. Due to the utilized energy regime of penetrating projectiles, LEIS sensitivity deteriorates with the thickness of the sample and therefore the useful information, i.e. the signal of probes which experienced only one scattering event within the material, requires to be treated with the utmost care. For extraction of this phenomenon, Monte Carlo simulations are usually utilized nowadays.
In presented work, the first chapter, 'Theoretical part', explains a necessary mathematical background of the problem, including the binary collision approximation, cross-section, the movement of a particle in the central field, discussion about nowadays most often utilized screening models and finally a complete derivation of the scattering integral. Furthermore, it provides a quick overview of the choice of projectiles and the description of respected parts spectral peak consists of. The end of the first chapter is devoted to the TRBS software.

In the second chapter, 'Practical part', we begin with the motivation for our work. Subsequently, a problem of the effects compromising the resulting spectrum is introduced. Next, we introduce a single-scattering model including both computational approaches of collisional events between the scatterer and target atom and an empirical evaluation from the simulated spectrum. Furthermore, TRBS predictions are challenged with our results to determine the validity of the model. Moreover, we expanded the possible applicability of the model for samples with different concentrations in their respected parts and for the different experimental set-ups alike. The last section demonstrates the expected struggling of the model when challenged with the application to the real experimental data.

Chapter 1

Theoretical part

1.1 Kinematics

In LEIS experiment, mono-energetic projectiles undergo collisions with target atoms, which results in both directional and energy change of incident particles. In the first approximation, these collisions are satisfactorily described by the model of binary collision from classical mechanics, as shown in Figure 1.1, implementing the conservation laws for energy as well as momentum.

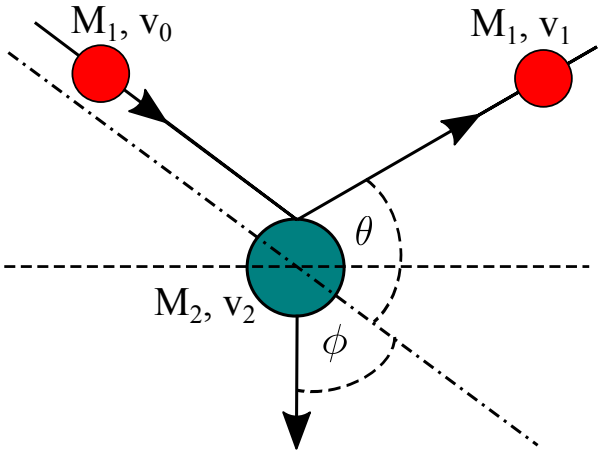

Figure 1.1: Approximation by binary collision.

In the case of static target atom with the mass M_2, conservation laws in parallel and perpendicular direction with respect to the incidence of projectile with mass M_1 and initial velocity v_0 are written as

$$\frac{1}{2}M_1v_0^2 = \frac{1}{2}M_1v_1^2 + \frac{1}{2}M_2v_2^2, \tag{1.1}$$

$$M_1v_0 = M_1v_1\cos\theta + M_2v_2\cos\phi, \tag{1.2}$$

$$0 = M_1v_1\sin\theta - M_2v_2\cos\phi. \tag{1.3}$$

Scattering and recoiling angle θ and ϕ determine, for given projectile-target combination, the resulting velocities v_1 (projectile) and v_2 (target) [1].

Eliminating ϕ and subsequently v_2, a ratio of resulting and initial velocity for projectile is obtained

$$\frac{v_1}{v_0} = \pm \frac{(M_2^2 - M_1^2 \sin^2\theta)^{1/2} + M_1 \cos\theta}{M_2 + M_1}. \tag{1.4}$$

For the case $M_2 > M_1$, where the plus sign holds, ratio stated above can be expressed by means of energies

$$E_1 = \left[\frac{(M_2^2 - M_1^2 \sin^2\theta)^{1/2} + M_1 \cos\theta}{M_2 + M_1} \right]^2 E_0 = kE_0. \tag{1.5}$$

Kinematic factor - k - represents a part of initial energy E_0 of the projectile after the collision event and is determined by the projectile-target combination and scattering angle only. It is possible for a projectile to have final energy higher than the one obtained by kinematic factor. Such events occur in case of the particle experiencing two collisions where the sum of their scattering angles equals the scattering angle θ.

1.2 Cross-section and impact parameter

An ideal LEIS experiment assumes a constant flux of impinging particles Y_0 and a uniform number of atoms per unit layer N_A. The yield of detected particles Y backscattered under the angle θ into a differential solid angle of the detector $d\Omega$ centred around θ is proportional to **differential scattering cross-section** - $d\sigma(\theta)/d\Omega$ - giving the formula

$$\frac{d\sigma(\theta)}{d\Omega}\, d\Omega\, N_A = Y/Y_0. \tag{1.6}$$

From a practical point of view, solid angle of detector Ω is small in backscattering experiments (10^{-2} and smaller [1], [2]), hence a **scattering cross-section** is defined as

$$\sigma(\theta) = \frac{1}{\Omega} \int_\Omega \frac{d\sigma}{d\Omega}\, d\Omega, \tag{1.7}$$

mathematically representing an average of differential cross-sections within Ω. Substituting from Equation 1.7 into Equation 1.6, the detected yield Y is given as

$$Y = \sigma(\theta) \Omega N_A Y_0, \tag{1.8}$$

showing that scattering-cross section has dimensions of an area.

Collision event of the projectile on a target atom can be described by the problem of a particle in central field, where the kinetic energy of scatterer is conserved. The perpendicular distance between the path of incoming projectile and a parallel line passing through the nucleus of target atom is defined as **impact parameter** - b - as shown in Figure 1.2.

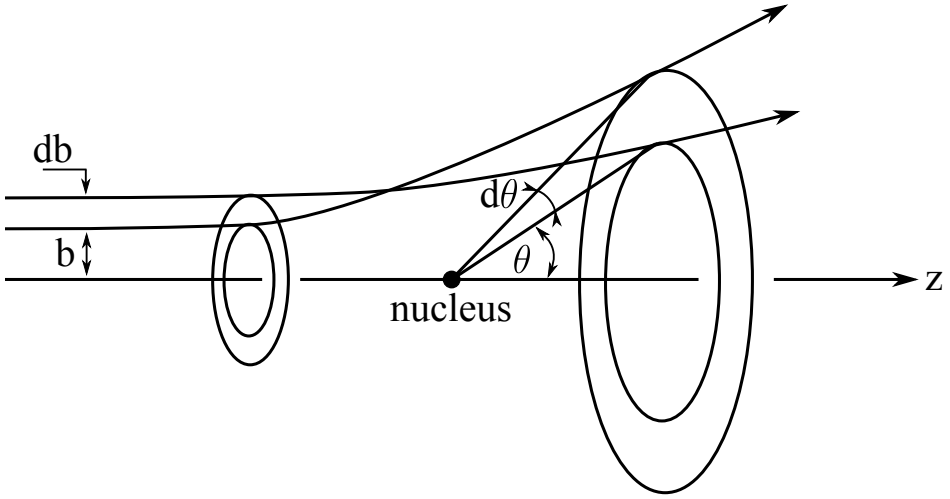

Figure 1.2: The dependence of scattering angle on the impact parameter.

Particles with impact parameters in the interval of $(b + db)$ will be scattered in the angular interval $(\theta + d\theta)$. Central field yield a total symmetry around the axis, hence

$$2\pi\, b\, db = -\sigma(\theta)\, 2\pi\, \sin\theta\, d\theta, \tag{1.9}$$

where $\sigma(\theta)$ is now a proportionality constant between b and θ. Minus sign indicates that an increase of impact parameter results in smaller scattering angle.

Scattering cross-section was so far treated as an enigmatic proportional constant relating impinged and detected particles or impact parameter and its corresponding scattering angle. In the following text, a precise relation to the scattering angle will be stated. Bold font in the equations denotes the vector of respected physical quantity.

1.3 Central force

As mentioned in the previous chapter, collision event can be described by the problem of a particle in the central field. Only a case without recoiling of the target atom - a one-body formulation - will be described.

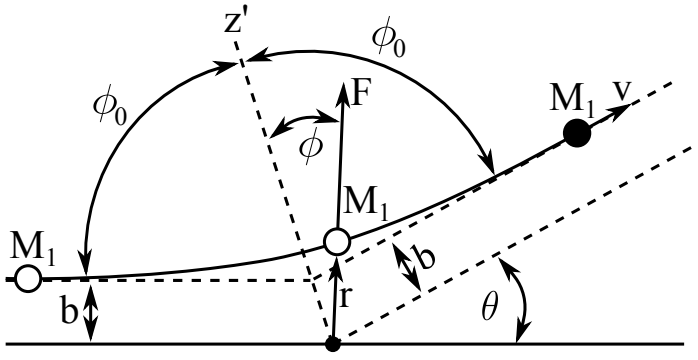

Figure 1.3: Particle scattering from a point charge of target nucleus.

As shown in Figure 1.3, an incoming particle M_1 with impact parameter b, charge Z_1e and velocity v approaches the target atom in the origin O with the charge Z_2e. At a distance r, Coulomb repulsive force is written as

$$F = k\frac{Z_1 Z_2 e^2}{r^2}, \tag{1.10}$$

where k is Coulomb constant. The total change in momentum of the particle $\Delta\boldsymbol{p} = \boldsymbol{p}_{\text{final}} - \boldsymbol{p}_{\text{initial}}$ is along the z' axis.

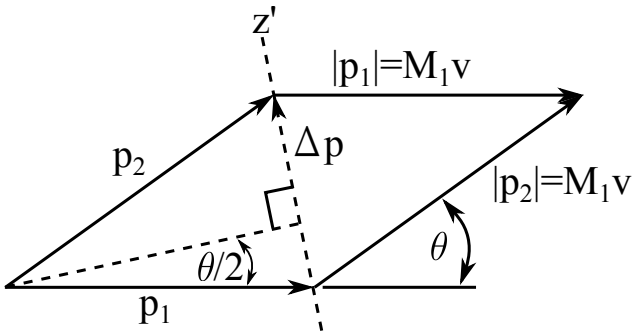

Figure 1.4: Particle scattering from a point charge of target nucleus. Acquired from [1].

The isosceles triangle in Figure 1.4 leads to an expression

$$\Delta p = 2M_1 v \sin(\theta/2). \tag{1.11}$$

Note that the absolute value of momentum before and after scattering does not change in central field one-body formulation.

Newton's law describes the momentum of particle as

$$d\boldsymbol{p} = \boldsymbol{F}dt. \tag{1.12}$$

Taking into consideration that total change of the momentum is along the z' axis, it could be calculated by the integration of radial component of Coulomb force

$$\Delta p = \int_{\phi_1}^{\phi_2} F\cos\phi\, dt = \int_{\phi_1}^{\phi_2} F\cos\phi\, \frac{dt}{d\phi}\, d\phi, \tag{1.13}$$

where, according to Figure 1.3, $\phi_1 = -\phi_0$ and $\phi_2 = \phi_0$. Transferring from dt to $d\phi$ results in the additional term $dt/d\phi$ within the integral, which allows to entangle the change in momentum with angular momentum as follows:
particle incoming from the infinity has angular momentum $M_1 vb$. For the entire duration of repulsive force, angular momentum is written as $M_1 r^2 d\phi/dt$ and this equality gives an expression

$$\frac{dt}{d\phi} = \frac{r^2}{vb}. \tag{1.14}$$

Substituting the right side and F from Equation 1.11 into Equation 1.13 yields

$$\Delta p = \frac{Z_1 Z_2 r^2}{vb}\int_{\phi_1}^{\phi_2} \cos\phi\, d\phi. \tag{1.15}$$

Taking into the consideration $2\phi_0 + \theta = 180°$ and substitution of Δp from Equation 1.11 binds the impact parameter b with kinetic energy E and scattering angle θ.

$$b = \frac{Z_1 Z_2 e^2}{M_1 v^2} \cot\frac{\theta}{2} = \frac{Z_1 Z_2 e^2}{2E} \cot\frac{\theta}{2}. \tag{1.16}$$

Finally, inserting obtained formula into Equation 2.3 using identity $\sin\theta = 2\sin(\theta/2)\cos(\theta/2)$ and $d\cot(\theta/2)/d\theta = -1/2\sin^2(\theta/2)$ results in

$$\sigma(\theta) = \left(\frac{Z_1 Z_2 e^2}{4E}\right)^2 \frac{1}{\sin^4(\theta/2)}. \tag{1.17}$$

This is scattering cross-section originally derived by Ernst Rutherford. One-body formulation assumes fixed scattering center without energy loss of the scatterer, however, projectile loses a portion of energy after the collision described by Equation 1.5. Because of this fact, the target atom cannot remain fixed during the mutual interaction and is recoiled from its original position. Problem leads to two-body formulation requiring more sophisticated approach, which is beyond the scope of this work. Detailed mathematical description along with the transformation between these two formulations is given in [1].

1.4 Scattering potential

The required information for the next two sections was obtained from [3].
Interaction between projectile and target atom in LEIS regime is an interaction between two charged particles (nuclei) influenced by their electron clouds, hence the pure Coulomb potential of a nucleus

$$\varphi_C = k\frac{Ze}{r} \tag{1.18}$$

has to be weakened. It is convenient to describe an electron screening by a function which depends only on the interatomic distances between colliding particles. Such is nowadays generally treated according to **screening function** - ϕ - proposed either by **Molière** [13] - derived from Thomas-Fermi model of an atom, hence often abbreviated as **TFM** - or **Ziegler-Biersack-Littmark** (**ZBL**) [14] - fitting curve of potentials computed for an 522 randomly chosen atomic pairs. Screening functions are expressed as a sum of exponentials

$$\Phi_{\mathrm{TFM}}(r) = 0.35e^{-0.3r/a} + 0.55e^{-1.2r/a} + 0.10e^{-6.0r/a} \tag{1.19}$$

and

$$\Phi_{\mathrm{ZBL}}(r) = 0.1818e^{-3.2r/a} + 0.5099e^{-0.9423r/a} + 0.2802e^{-0.4029r/a} + 0.02817e^{-0.2016r/a} \tag{1.20}$$

where r is the **distance** between colliding particles and a is a parameter called **screening length** and differs for respected model. In case of Molière screening, Firsov screening length, defined as

$$a_{\mathrm{F}} = \frac{0.88534a_0}{(Z_1^{1/2} + Z_2^{1/2})^{2/3}} \tag{1.21}$$

is used, whereas for ZBL a Universal - also simply denoted as ZBL - screening length is implemented

$$a_{\mathrm{ZBL}} = \frac{0.88534a_0}{Z_1^{0.23} + Z_2^{0.23}}. \tag{1.22}$$

Constant a_0 is the radius of the first electron orbit in a hydrogen atom - the first **Bohr radius**. In order to find a better agreement with experimental data, screening length is often modified by **screening length correction** - c_a - smaller than unity and a new screening length $a' = c_a a$ is obtained. As a result, nuclei screening is enhanced, i.e. screening function becomes steeper, as shown in Figure 1.5.

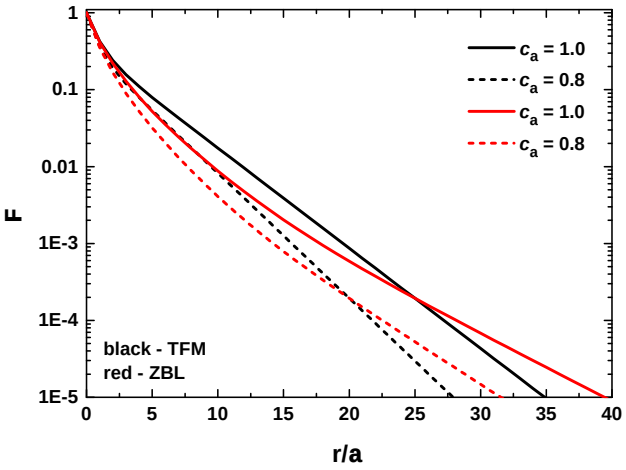

Figure 1.5: Comparison between Molière and ZBL screening for uncorrected $c_a = 1.0$ and corrected $c_a = 0.8$ screening length a. Horizontal axis denotes the ratio of interaction distance r to screening length a chosen in accordance with the model.

The resulting screened potential between projectile and target atom is henceforth in the form

$$\varphi = \varphi_C \, \Phi(r/a). \tag{1.23}$$

and will naturally influence scattering cross-section $\sigma(\theta)$ via the relation $F = Z_p \cdot e \cdot E = Z_p \cdot e \cdot (-grad\,\varphi)$, where Z_p is the atomic number of the projectile and F is the Coulomb force in Equation 1.10. Another consequence of screening is different values of scattering angle θ for the same impact parameter b: weaker potential scatters particles under smaller scattering angle than unscreened one.

1.5 Scattering integral

Description of projectile's trajectory during the scattering from the target atom is conducted by the solving of **scattering integral**. To begin with, Lagrangian of the system, subtraction of potential energy V from the kinetic energy T, is established in the form

$$\mathcal{L} = T - V = \frac{1}{2}(M_1 \dot{\boldsymbol{r}}_1^2 + M_2 \dot{\boldsymbol{r}}_2^2) - \varphi(|\boldsymbol{r}_1 - \boldsymbol{r}_2|) \tag{1.24}$$

where $\boldsymbol{r}_1/\boldsymbol{r}_2$ are coordinates of projectile and target atom, respectively. More convenient approach to the problem is to find a solution in center-of-mass (CM) system, where position of the CM is placed at zero

$$\boldsymbol{r}_{\mathrm{CM}} = M_1 \boldsymbol{r}_1 + M_2 \boldsymbol{r}_2 = 0. \tag{1.25}$$

Introducing a vector of relative displacement drawn from projectile to target atom

$$\boldsymbol{r} = \boldsymbol{r}_1 - \boldsymbol{r}_2 \tag{1.26}$$

enables to express the coordinates in the form

$$\begin{aligned} \boldsymbol{r}_1 &= \frac{A}{1+A}\boldsymbol{r} \\ \boldsymbol{r}_2 &= -\frac{A}{1+A}\boldsymbol{r} \end{aligned} \tag{1.27}$$

where $A = M_2/M_1$. Substituting obtained coordinates into Equation 1.24 results in expression

$$\mathcal{L} = \frac{1}{2}\mu\dot{\boldsymbol{r}}^2 - \varphi(|\boldsymbol{r}|) \tag{1.28}$$

with $\mu = M_1M_2/(M_1+M_2)$ representing **reduced mass** - mass of a hypothetical particle moving in central field. Further simplification of the problem is utilized by applying the conservation laws for **angular momentum** $\boldsymbol{L} = \boldsymbol{r} \times \boldsymbol{p}$ and **total energy** E. Since $\boldsymbol{r}$ is perpendicular to $\boldsymbol{L}$ which remains constant, particle is moving in the plane perpendicular to $\boldsymbol{L}$. Switching to polar coordinates r and θ and placing center of the force in zero, Equation 1.28 becomes

$$\mathcal{L} = \frac{1}{2}\mu(\dot{r}^2 + r^2\dot{\theta}^2) - \varphi(r). \tag{1.29}$$

Lagrange equation with generalized variable q

$$\frac{d}{dt}\left(\frac{\partial\mathcal{L}}{\partial\dot{q}}\right) = \frac{\partial\mathcal{L}}{\partial q} \tag{1.30}$$

results for considered case in a pair of equations

$$\begin{aligned} \frac{d}{dt}\left(\frac{\partial\mathcal{L}}{\partial\dot{r}}\right) &= \frac{\partial\mathcal{L}}{\partial r}, \\ \frac{d}{dt}\left(\frac{\partial\mathcal{L}}{\partial\dot{\theta}}\right) &= \frac{\partial\mathcal{L}}{\partial\theta}. \end{aligned} \tag{1.31}$$

From the latter is obtained

$$\frac{d}{dt}(\mu r^2\dot{\theta}) = 0 \Rightarrow \mu r^2\dot{\theta} = const. = L, \tag{1.32}$$

which confirms the conservation law for angular momentum. Substitution of Equation 1.32 in the expression for energy

$$E = T + V = \frac{1}{2}\mu(\dot{r}^2 + r^2\dot{\theta}^2) + \varphi(r) = \frac{1}{2}\mu\dot{r}^2 + \frac{L^2}{2\mu r^2} + \varphi(r). \tag{1.33}$$

Expressing the distance dependence on time from Equation 1.33

$$\dot{r} = \frac{dr}{dt} = \sqrt{\frac{2}{\mu}(E - \varphi(r)) - \frac{L^2}{\mu^2 r^2}} \tag{1.34}$$

leads after integrating to an implicit time dependence on the distance between hypothetical particle with mass μ and the force center

$$t = \int \frac{dr}{\sqrt{\frac{2}{\mu}(E - \varphi(r)) - \frac{L^2}{\mu^2 r^2}}} + const. \tag{1.35}$$

The last step is to substitute $\dot{\theta}$ from Equation 1.32 to obtained time equation, which results in

$$\theta = \int \frac{Ldr/r^2}{\sqrt{2\mu(E - \varphi(r)) - \frac{L^2}{r^2}}} + const. \tag{1.36}$$

Angular momentum is a product of vector multiplication $\boldsymbol{L} = \boldsymbol{r} \times \boldsymbol{p}$, i.e. it considers only the part of vector $\boldsymbol{r}$ which is perpendicular to $\boldsymbol{p}$. Perpendicular distance from the momentum vector was previously denoted as impact parameter b. Recalling general expression $p = \sqrt{2mE}$, angular momentum could be rewritten in $L = b\sqrt{2\mu E}$ and finally the scattering integral is derived:

$$\theta = \int \frac{bdr/r^2}{\sqrt{1 - \varphi(r)/E - b^2/r^2}} + const. \tag{1.37}$$

The result of scattering integral is the scattering angle. It is important to realize that $\varphi(r)$ used for the derivation is a scattering potential discussed in previous section. Thus, implementing the screening models, alternatively some corrections to them, will have an impact on the result.
In presented work, however, a demand for inverse computation is needed - for chosen scattering angle an impact parameter, hence cross-section is demanded. Such computation is not a trivial task and was not utilized in the following pages by author himself - desired values of cross-sections were obtained from on-line program LEIS Energy Calculator [16], which enables to perform the computation for either of discussed screening models introduced in previous section, however, without the option of screening length correction.

1.6 Stopping power

Penetrating projectile loses its kinetic energy either via collisions with target atoms - **elastic energy loss** - or via interaction of electron clouds - **inelastic energy loss**. The sum of these mechanisms is denoted as **total energy loss**

$$\Delta E = \Delta E_n + \Delta E_e \tag{1.38}$$

where ΔE_n is nuclear (elastic) and ΔE_e is electronic (inelastic) energy loss.

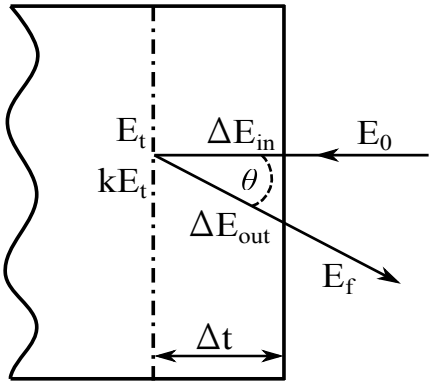

Figure 1.6: Energy loss of a projectile during its propagation in the sample.

As shown in Figure 1.6, a projectile with kinetic energy E_0 loses a part of this energy during its propagation through the sample. In the depth Δt, the energy of the projectile equals

$$E_t = E_0 - \Delta E_{in}, \tag{1.39}$$

where ΔE_{in} is energy lost on inward path. After the scattering under θ, a projectile begins to propagate with kinetic energy kE_t with k being the kinematic factor from Equation 1.5. On outward path, energy loss is denoted as ΔE_{out} and projectile emerges with final energy

$$E_f = kE_0 - k\Delta E_{\mathrm{in}} - \Delta E_{\mathrm{out}}. \tag{1.40}$$

Energy loss is proportional to the depth of penetration, since interactions of electron clouds / scattering events become more abundant, and therefore **stopping power** - S - is defined as an energy loss per the length of trajectory

$$S = dE/dx, \tag{1.41}$$

with the unit of eV/Å. Similarly, as for an energy loss, stopping power could be either nuclear or electronic. In practice, to obtain total energy loss, S has to be integrated along the entire trajectory of a projectile to determine the energy loss. For the analysis of thin films, energy loss is, to a good approximation, linearly dependent on the path length l:

$$\Delta E = \int_0^l \frac{dE}{dx} dx \cong \frac{dE}{dx} \cdot l \tag{1.42}$$

In Equation 1.40 the term kE_0 corresponds to scattering from the outermost atomic layer, hence depends not on the particle trajectory in the solid, contrary to remaining terms, which determine the full-width at half maximum (FWHM) of the spectrum:

$$\Delta E = k\Delta E_{\mathrm{in}} + \Delta E_{\mathrm{out}}. \tag{1.43}$$

Equation might be written in terms of stopping power and path length of backscattered projectile. According to Figure 1.6 total energy loss is written as

$$\Delta E = \Delta t \left[k \frac{dE}{dx}\bigg|_{\mathrm{in}} + \frac{1}{|\cos\theta|} \frac{dE}{dx}\bigg|_{\mathrm{out}} \right]. \tag{1.44}$$

Since the total path length of the projectile in Equation 1.44 equals to $t(1+1/|\cos\theta|)$, described calculation does not include multiple scattering events, which would result in prolonging of the trajectory. These stochastic events cannot be analytically described, hence Monte Carlo simulations are usually implemented for their description to some extent.

1.7 Projectiles, experimental set-up and detected spectra

In classical LEIS experiment, atoms of noble gasses (He^+, Ne^+, Ar^+) with energies between 0.5 keV and 10 keV are used as probes due to their non-reactive nature. Henceforth, any chemical modification of the samples are eliminated. Utilized energy regimes allows to investigate the samples up to 10 nm [7]. However, investigation with protons were reported as well [5], [6]. Experimental set-ups with the incident angle (with respect to surface normal) smaller than 60° and scattering angle typically 140° ensure almost exclusive binary collisions of impinging projectiles from surface atoms [8], [9].

Two LEIS experimental approaches can be utilized:

Electro Static Analyser (ESA), enabling to detect only those projectiles which remained in ionized state after leaving the sample surface. Since ions of noble gasses backscattered from beneath the outermost layer often lose their charge [9], ESA-LEIS is extremely sensitive to the elemental composition of the surface.

In contrary, Time-of-Flight (ToF) experiments collect both ions and neutrals, which is a desired asset for studying the thickness as well as the stopping power, see section 1.6, in the clean samples and compounds.
The difference between experimental spectra obtained by mentioned methods is shown in Figure 1.7. Whereas ESA-LEIS spectrum for thick sample consisting of pure polycrystalline copper - Cu - exhibits a Gaussian-like peak shape, spectral shape of ToF experiment does not even have a defined boundary towards lower final energies.

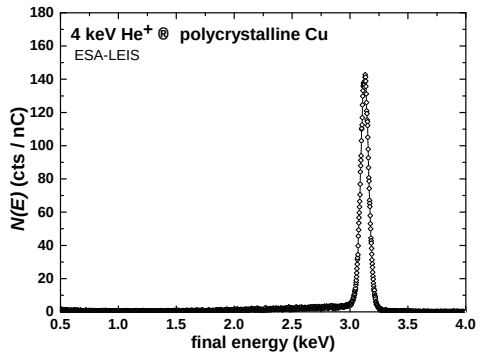

(a) ESA-LEIS spectrum. Courtesy of Stanislav Průša.

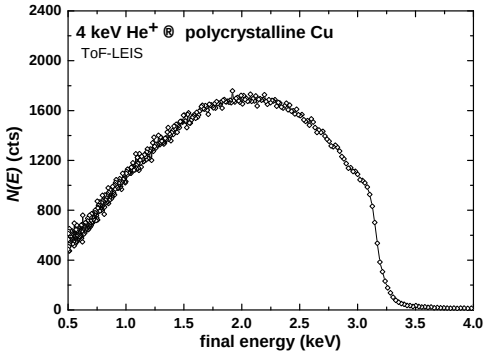

(b) ToF-LEIS spectrum.

Figure 1.7: The difference between experimental spectra obtained either by Time-of-Flight or ElectroStatic Analyser for He projectiles with primary energy of 4 keV backscattered under $(135 \pm 1)°$ from polycrystalline Cu.

1.8 Description of the spectrum

In this work, ToF spectra are discussed only. Before continuation, an important terms describing the spectral shape of the peak need to be defined. These are shown in Figure 1.8.

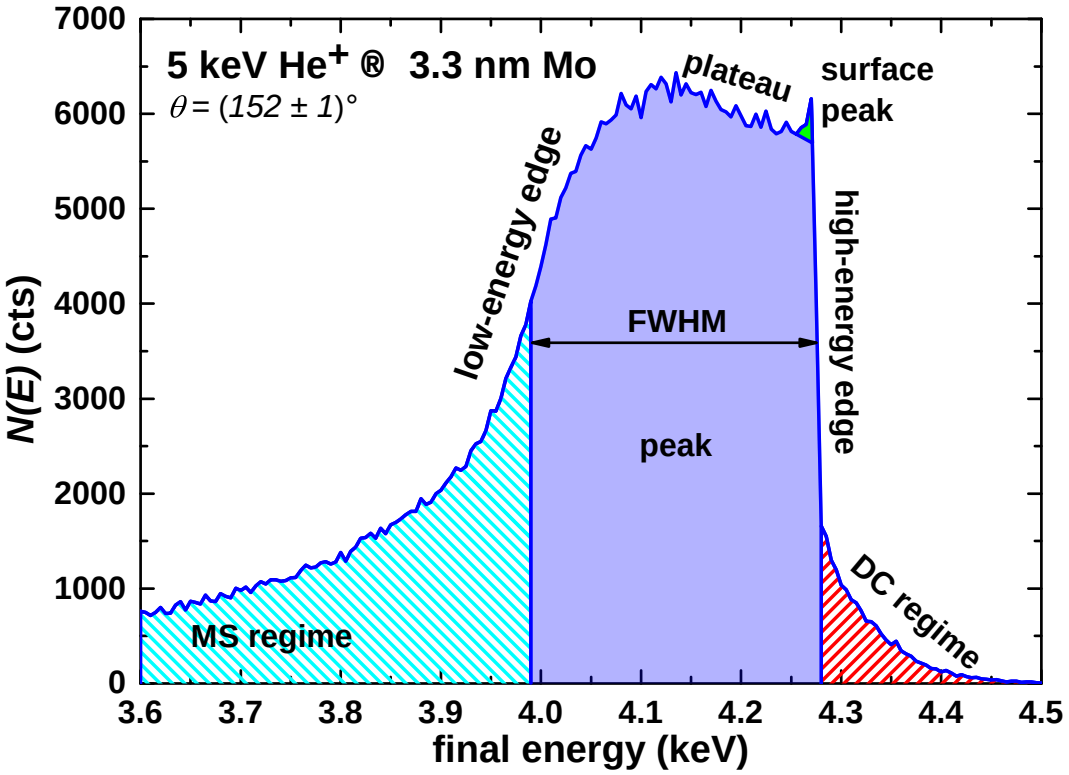

Figure 1.8: Important terms for spectral shape description.

Area denoted as DC (double-collisions) regime represents the projectiles which experienced two scattering events and emerged with final energy higher that the one predicted by kinematic factor, as discussed in section 1.1. In contrary, MS (multiple-scattering) regime is an outcome of the events when projectile scattered numerous times from the target atoms. The surface peak is a unique feature of the spectrum in LEIS regime and will be discussed to further extent in subsection 2.3.5. Area denoted as 'peak' or 'FWHM' (full width at height maximum) is, in an ideal case, supposed to consist only from single-scattered particles. However, LEIS peaks are mostly products of MS and DC events towards the lower final energies. Plateau of the peak is connected with the energy scaling of the cross-section. High- (low-) energy edge describes the beginning (end) of the peak. The latter becomes highly influenced by MS events, hence is visibly less skewed than the first one.

1.9 TRBS

TRim for BackScattering (TRBS), a descendant of TRIM (TRansport of Ions in Matter) [14], is a software implementing Monte Carlo code for simulation of ToF spectra. It enables the user to simulate energy spectra of particles backscattered within chosen detector angular interval, even with additional information about the number of collisions particles experienced during their penetration within the sample. Energy and angular spectra for transmitted particles and energy spectra of implanted particles could be opt for as well. The incident beam of projectiles is perpendicular to the surface of the sample by default, contrary to TRIM, where the angle of incidence is of user's choice. Different mathematical approaches as well as different conditions for scattering implemented in the software [12] significantly decreased the computational time. In addition to the option of correcting the electronic stopping power, latter program also enables to correct screening length, see section 1.4, and determine the conditions for scattering.

1.9.1 Stopping power correction

TRBS uses so-called 'Universal Stopping', as defined in [14]. Values often do not match experimentally collected data, which are available in SRIM (Stopping and Ranges of Ions in Matter) database [15], and the discrepancies between experimental and simulated spectra are becoming more significant with decrease of primary projectile energy. For this reason, an empirical **stopping power correction** - c_e - has to be implemented to find an agreement between two them. The parameter is higher than unity implying that penetrating particles are slowed down more within the sample than predicted by ZBL.

1.9.2 Screening length correction

As introduced in section 1.4, screening length correction c_a is often introduced to find a better fit between simulated and experimental spectra. Tuning of screening length is often a necessity due to the fact that both discussed screening functions tend to underestimate the screening effect of electron clouds on target nuclei for larger impact parameters, in other words smaller scattering angles for the same energy of the particle. In practical terms such fitting process leads to lowering of the height of the spectrum, more profoundly the peak area.

1.9.3 Cut-off angle

Tunable parameter determining which collisions are to be treated in Monte Carlo computation as scattering events is called **cut-off angle**, defined in TRBS as $\sin(\vartheta/2)$ with θ being the scattering angle. Collisions below the input value are included in the final simulation as an analytical correction. Discussed parameter has a significant influence on the computational speed, it is, however, advised to choose it in such fashion that the mean number of collisions per layer is above 10 for backscattered particles. In general, no reasonable MS events should be underestimated by ensuring stated number. Cut-off angle is the major decisive factor when it comes to investigation of the number of collisions, which a backscattered projectile underwent in the sample.

Chapter 2

Practical part

2.1 Motivation

He who defends everything, defends nothing.

- Frederick the Great

The entire idea behind the presented work was born from an investigation of LEIS depth resolution conducted by Duda in [11]. Sample consisting of alternating 3.3 nm thick molybdenum - Mo - layer and 11 nm thick silicon - Si - layer was sputtered by argon projectiles and subsequently LEIS spectra were collected.

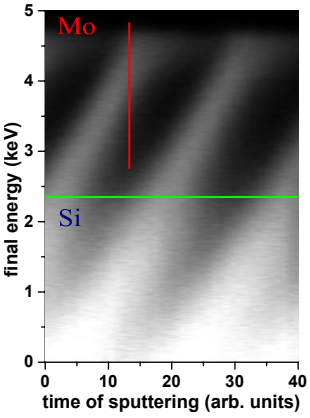

Figure 2.1: Spectra of MoSi multilayers. Acquired and adjusted from [11].

The results are shown in the form of bitmaps in Figure 2.1: the vertical axis represents the final energy of detected particles, whereas the horizontal one is connected with time of sputtering. The intensity of the map represents the intensity of the signal. The layer of interest was the Mo one, marked with the red line, hence in our work, we will discuss primarily Mo peak. Below the green line projectiles backscattered from Si were detected, but it is of no practical importance concerning the problems discussed later. An ever-asked question about how to eliminate the contribution of MS events from Mo spectra was answered by the introduction of an exponential fit to MS events and its subsequent subtraction from the spectrum. Despite its undeniable usefulness and straightforward applicability, the method was designed for practical purpose and physics behind it might be difficult to grasp and connect with the events occurring during the projectile propagation through the sample. In presented work, we attempt to discuss the latter, which is, unfortunately, achieved by the loss of immediate practical application.

2.2 Slabs simulation

As discussed in the previous sections, in LEIS experiments *single-scattering* (SS) events under the backscattering angle θ are becoming minor due to *double-collision* (DC) and *multiple-scattering* (MS) events which are dominating as the projectiles are emerging from deeper layers of the sample. Demonstration of mentioned phenomenons is shown in Figure 2.2, when the 3.3 nm thick Mo layer was divided into 10 equal slabs. The number of slabs was not chosen deliberately and is discussed in subsection 2.3.1. Sharp, Gaussian-like peaks indicating SS events are gradually on a decrease, while DS and MS become more profound as the projectile penetrates deeper into the sample. Peaks are becoming broader and shorter until the last remains of SS event almost vanish approximately at final energy of 4 keV. Only particles experiencing one scattering event within the sample bring useful information about the sample, as they are unspoiled by mentioned compromising DC and MS effects. We used depicted Mo peak several times in this work to describe different phenomena and procedures. It was utilized to help the reader to concentrate on discussed topics rather than being distracted by the different examples every time a new problem occurs.

The influence of tunable parameters introduced in section 1.9 will now be discussed in greater detail. To obtain the desired information, TRBS software enables to opt for collisional distribution, as mentioned in the same section. However, it is important to note that these spectra have only 100 bins, where one bin represents 1% of the primary energy. Such feature prevents the software from reproduction of the high energy edge of the peak, as will be seen in section 2.4. Nevertheless, the general shape and behaviour of experimental spectra are satisfactorily predicted.

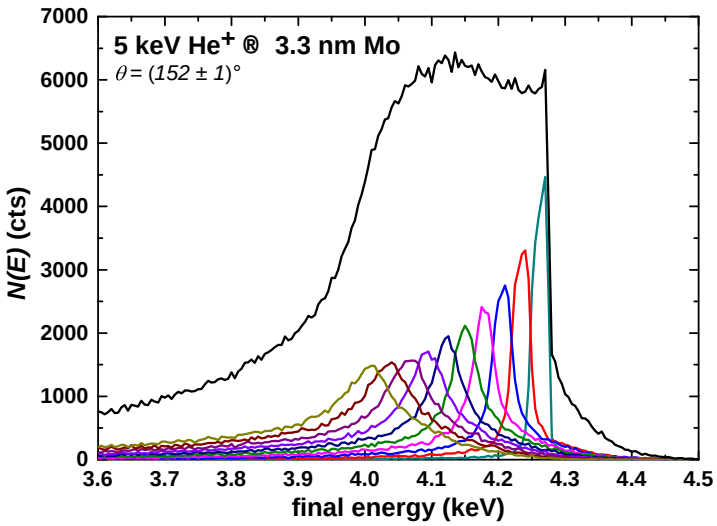

Figure 2.2: TRBS simulation of Mo layer divided into 10 slabs of 3.3 Å thickness each. Sharp, Gaussian-like peaks visible in the beginning of the spectrum are being surpassed as the projectile penetrates deeper into the sample. In contrary, DS and MS events become more profound.

2.2.1 How does S_e, c_a and ϑ influence single-scattering?

Increasing the stopping power value corresponds to higher energy loss of the projectile while propagating through the sample. Simulations for different S_e, adjusted by c_e, are shown in Figure 2.3. Their actual value is of no importance for our work. We observe a decrease in the peak - corresponding to the lowering of entire spectrum - and its gradual broadening towards the lower final energies. Comparison of the spectral shape provides comforting information - stopping power tuning just shifts the energy border from which the particle is still able to reach the detector. It does not cause a higher occurrence of the MS events in the deeper layers, since the SS prediction broadens together with the entire experimental peak.

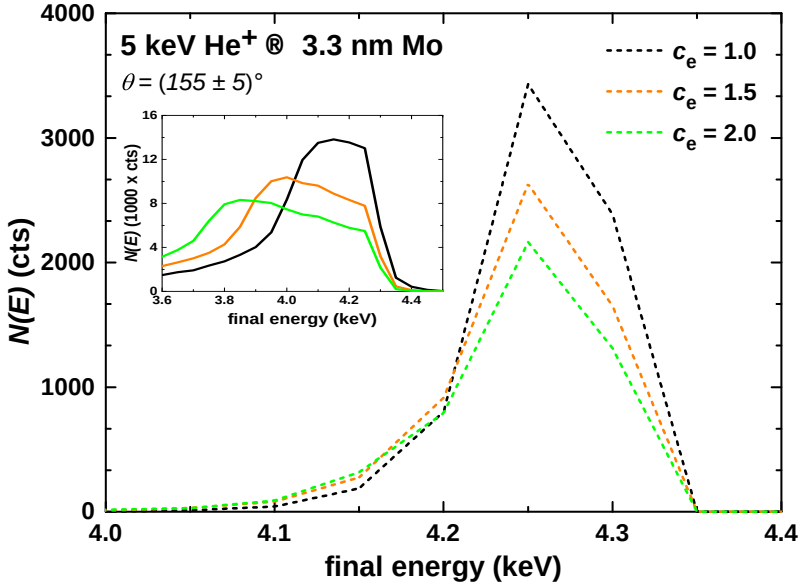

Figure 2.3: Influence of tuning electronic stopping power on single-scattered particles contribution as well as on an entire spectrum depicted in the inset.

Scattering potential adjusted by c_a results in total lowering of SS yield, as depicted in Figure 2.4. The height of the peak is decreasing, similarly as for tuning of S_e, but no broadening towards lower energies is pronounced. The position of the peak remains constant. General behaviour of the spectra shown in the inset of the figures was previously reported by Chenakin et al. in [10].

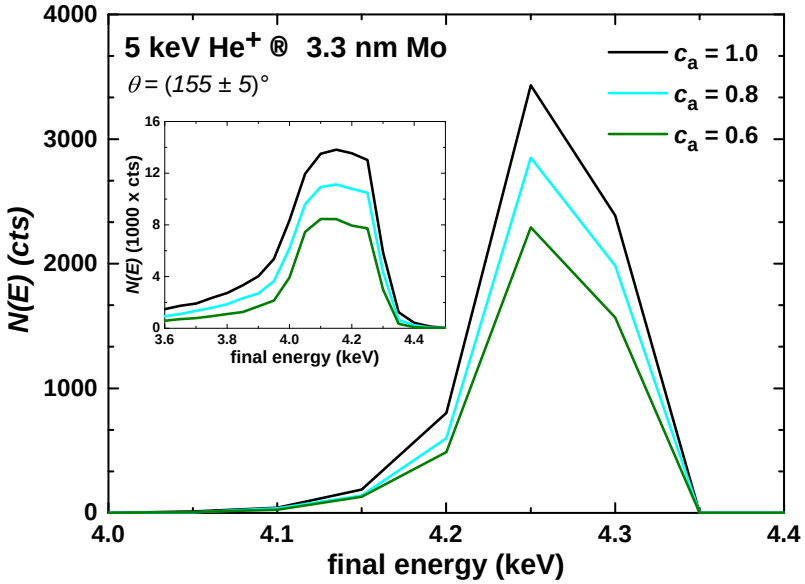

Figure 2.4: Influence of screening length correction on single-scattered particles contribution as well as on an entire spectrum depicted in the inset.

The choice of the last tunable parameter relevant for SS investigation proves to have the opposite effect on resulting spectra than adjustments in c_a as well as S_e. As could be observed from Figure 2.5, from 3.5° the TRBS spectrum does not drop below 4 keV, which implies that from certain choice of cut-off angle, the total yield of single-scattered particles is being increased without any further expansion towards lower energies.

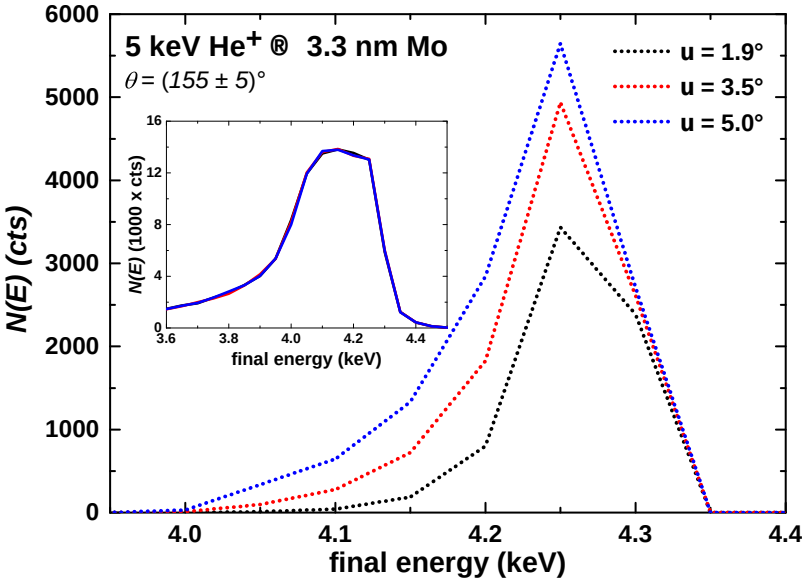

Figure 2.5: Influence of cut-off angle. on single-scattered particles contribution as well as on an entire spectrum depicted in the inset.

2.3 Single-scattering model foundations

Some part of a mistake is always correct.
- Siegbert Tarrasch

Contribution of particles which experienced only one scattering event to the total detected yield is possible to evaluate by the use of computer simulations. In case of TRBS, the resulting single-scattering spectrum is, for known stopping power and screening model, highly sensitive to the chosen cut-off angle, as already demonstrated. In other words, its shape is modified by the boundary angular restriction *up to which the scattering event is not considered to be scattering at all.*

In presented work, we propose an idea of a model implementing this boundary without a need for further simulation process. The goal of the model is to meet the TRBS predictions.

The investigation is aimed at samples consisting of various elements, different mutual combinations of these elements in respected areas of the sample, with the utilization of different detector angles and primary energy of He projectiles alike. Spectra simulated by TRBS using ZBL screening are denoted as 'experiment'. Scattering under angle θ will be always referred to as 'backscattering', while collisions under small angles will be denoted as 'scattering'.

2.3.1 Elimination of electronic stopping power

Our ideas will revolve around 5 keV He projectiles impinging on 3.3 nm molybdenum - Mo - sample and backscattering within the detector angular interval $(152 \pm 1)°$. Assuming the length of Mo lattice parameter $p = 314.7\,\text{pm}$ [18], the entire thickness of the sample can be estimated to consist of 10 Mo monolayers, i.e. 11 interfaces (discussed later in Figure 2.7). As seen in the Figure 2.6 (a), a particle backscattering from the last interface has the energy approximately 4.15 keV - end of yellow region - due to energy loss mechanisms of both electronic stopping on the path in - $S_{\text{e, in}}$ - and kinematic factor k for backscattering under angle θ. It loses the rest of the energy while propagating back towards the detector due to $S_{\text{e, out}}$ - end of blue region in Figure 2.6 (a) - emerging with the final energy of 3.99 keV. Note that the areas are not equally wide.

We propose a different view on the problem: let the particle from the last interface backscatter under the detector angle with energy 3.99 keV - the energy it was detected - instead of 4.15 keV. This assumption links the width of the experimental peak directly to the thickness of the sample. Furthermore, we consider $S_{\text{e, out}} = 0\,\text{eV/Å}$, i.e. we consider only yellow region during the particle's propagation through the sample. In such approximation, particle backscattered from the chosen interface is heading towards the detector with the same energy as it was detected in the experiment after it lost additional energy due to $S_{\text{e, out}}$. In this case, we are hypothetically increasing stopping power on the way in order to match the detected energies. Described line of thought is shown in Figure 2.6 (b).

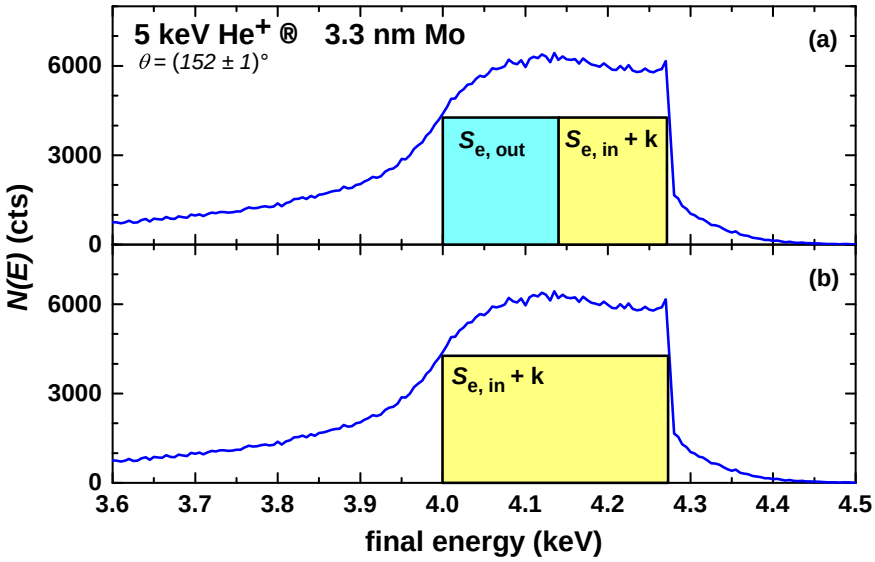

Figure 2.6: Assumption made for upcoming model. In the picture (a), the real mechanism of energy loss is depicted. Picture (b) represents the different point of view on the resulting experimental peak.

2.3.2 Scattering events restriction

The next step is to establish the rules for particle scattering. The idea is to compare the cross-section $\sigma(\vartheta)$ of different scattering angles ϑ to the cross-section of referential angle which denotes the boundary when the scattering event is to be neglected. We opted for $\vartheta = 1°$ as a referential angle. For our experiment, the value also matches the acceptance angle of the detector. Scattering angles were chosen up to the angle when the projectile loses 0.1% of its kinetic energy after the collision, which is calculated from kinematic factor and for He-Mo pair results in $\vartheta = 9°$. Angles were chosen with the step of 1°. We obtained a probability of scattering for angle ϑ

$$P_{(\alpha)} = \frac{\sigma(\vartheta = \alpha)}{\sigma(\vartheta = 1°)}; \;\; \alpha = 2°, 3°, \ldots, 9°. \tag{2.1}$$

Note that $\sigma(\vartheta = 1°)$ is a restriction stating that 1° collisions are not collisions, whereas $\sigma(\vartheta = \alpha)$ represents the benevolence of the model - which collisions are to be considered as no-collisions, but with respect to the referential case of 1°. All cross-sections were computed for energy $E_{\mathrm{ref}} = kE_0$, assuming that $P_{(\alpha)}$ is not influenced by the choice of E_{ref}, which could be taken deliberately from, for example, the middle of the experimental peak. Even though cross-section for a certain scattering angle scales linearly with the decreasing energy, i.e. depth of the sample, $P_{(\alpha)}$ is slightly increasing. As an example, $P_{(9°)}(E = 4.27\,\mathrm{keV}) = 0.0033$, whereas $P_{(9°)}(E = 4.0\,\mathrm{keV}) = 0.0032$. The ratio decreased by 3.1%. However, as we are showing later, this scaling has a negligible effect on the final result. Therefore we are proceeding with the assumption that $P_{(\alpha)}$ dependence on the depth need not be taken in the consideration, henceforth it remains constant. The values of probabilities were obtained from [16] and for computation, ZBL screening was utilized. Prior to stating the actual $P_{(\alpha)}$ values and their distribution, we need to explain the assumption for projectile propagation in the sample.

2.3.3 Weight function

The next step is to orchestrate the **weight function**: for particles backscattering from deeper interfaces larger scattering angles are tolerated due to the fact that such particles have more 'opportunities' - more interfaces to pass through - to be scattered again and re-routed to the acceptance angle of the detector. For a projectile backscattered under θ, scattering on the first interface is the most restricting - since the acceptance angle of the detector is only 1°, collisions under 2° result in preventing the particle from being detected. On the other hand, projectile scattered on the second interface under 3° has one more interface - the first one - to eventually deal with the situation and change projectile's trajectory back to the detector. Our procedure allows a scattering under the angle higher by 1° for every next interface. In conclusion, we have a restriction for 2° on the first interface and 9° for the eighth, the ninth and tenth interface in our Mo sample consisting of 11 interfaces. Taking into consideration both angular restrictions for respected interfaces as well as the number of interfaces through which the projectile has to propagate to reach the detector, the weight function is in the form

$$W(\alpha, i) = \sum_{i-1} P_{(\alpha)} \cdot (1 - (P_{(2^\circ)} - P_{(\alpha)}))/(i-1); \quad i \geq 2,\ \alpha = 2^\circ, 3^\circ, ..., 9^\circ. \tag{2.2}$$

The term $(i-1)$ describes the number of interfaces through which the projectile has to pass to emerge in the spectrum. Expression $(1-(P_{(2^\circ)}-P_{(\alpha)}))/(i-1)$ for $i = 2$ and $\alpha = 2^\circ$, i.e. backscattering from the second interface, is truly putting the highest restriction on the scattering from the first interface - probabilities $P_{(\alpha)}$ are equal and $i - 1 = 1$, hence $P_{(\alpha)}$ after the sum remains unchanged. Obtained values of $P_{(\alpha)}$ and their distribution are in Table 2.1.

$interface/\alpha$	$P_{(\alpha)}$
1/2°	0.1770
2/3°	0.0630
3/4°	0.0300
4/5°	0.0168
5/6°	0.0104
6/7°	0.0069
7/8°	0.0049
8/9°	0.0036
9/9°	0.0036
10/9°	0.0036

Table 2.1: The number of interfaces, their corresponding scattering angle α and scattering probabilities $P_{(\alpha)}$. Because we tolerate scattering from 2° up to 9° with the step of 1°, but the number of interfaces is 10 for the particle backscattering from the last interface, the deepest 3 interfaces (2 monolayers) are tolerated for the same angle.

An example of angular tolerance for respected interfaces (black points) is shown in Figure 2.7. A projectile was backscattered from 10nth interface. Subsequently, it underwent 3 scattering events on interfaces 9, 6 and 3. In case that the scattering event occurred under the angle smaller or equal the depicted angular restriction for each interface - 9°,

7° and 4°, respectively - the events are not taken into consideration as collisions and we assume the straight trajectory after backscattering. The next part contains a simplified description of the yield scaling with respect to the cross-section.

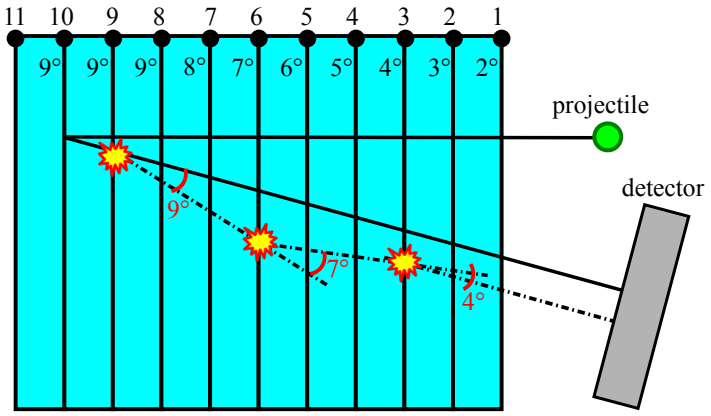

Figure 2.7: Schematic depiction of scattering from the 10th interface. For each interface, angular tolerance is shown.

2.3.4 Number of particles

The number of projectiles detected from each subsequent interface, without $W(\alpha, i)$ in mind, is derived from the previous interface as follows:

1. for detector angle, the cross-section for deeper and cross-section for the previous interface are compared;

2. the number of detected projectiles from the previous interface is multiplied by this ratio:

$$n'_i = n_{i-1} \cdot \left. \frac{\sigma_i}{\sigma_{i-1}} \right|_{\theta}. \tag{2.3}$$

Instead of the ratio of neighbouring cross-sections (σ_i/σ_{i-1}) a replacement by the ratio of neighbouring total detected yields ($N(E)_i/N(E)_{i-1}$) obtained from the spectrum can be utilized. Comparison of this nature binds more tightly to the experiment and offers other possibilities which are discussed in section 2.5. The remaining question to answer is about the choice of the starting point of the SS model.

2.3.5 Starting point

In Figure 2.8 it is clearly visible that on the bottom of the high-energy edge of Mo peak rises a skewed step of particles with energy higher than kE_0 - these correspond to double collisions, as discussed at the end of section 1.1. Therefore, these can be safely subtracted from the edge, as depicted in the figure. Moreover, the visible surface peak should be also subtracted, since it corresponds to the projectiles backscattered exclusively from the first (eventually the second) interface [17] and this phenomenon does not occur further in the sample. Thus we obtained the *yield starting point*. For *energy starting point*, we take the energy corresponding to the top of the surface peak, in a presented case $E = 4.27$ keV. Elimination of the surface peak is executed by linear interpolation of the plateau right behind the peak, as shown in the same figure.

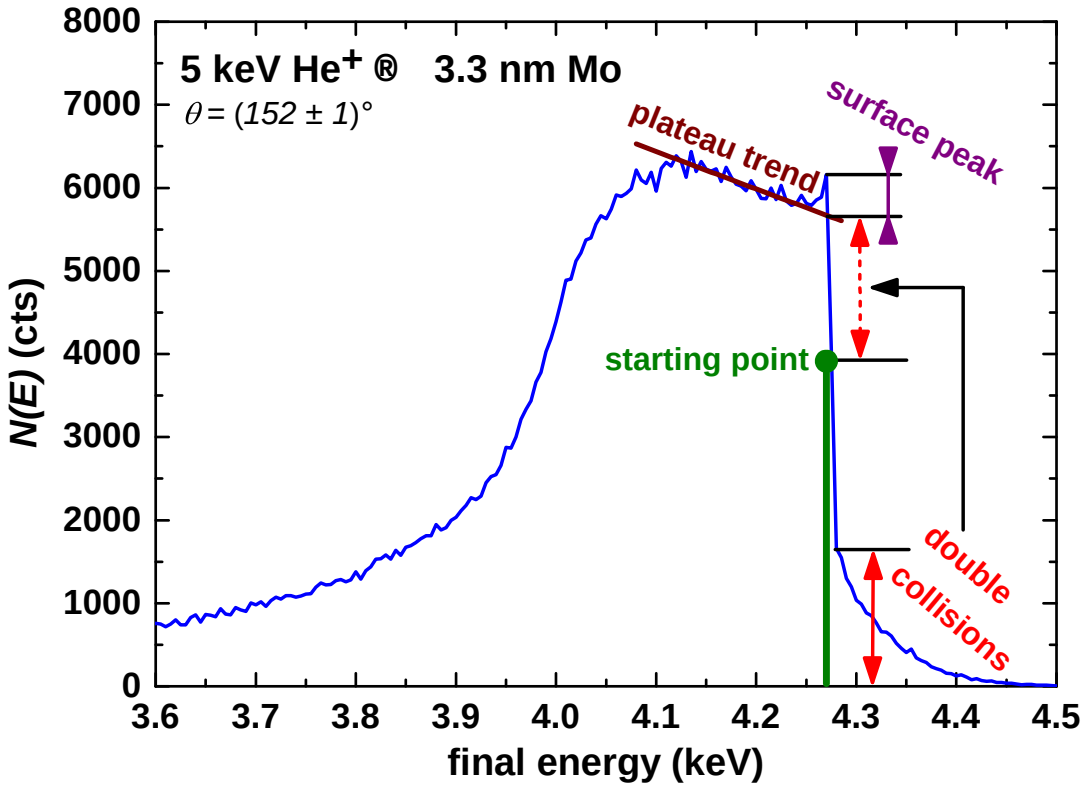

Figure 2.8: Subtraction of double collisions as well as the surface peak from the experiment. The procedure allows for establishing the starting point of the SS model. Green line and point denote both the position and the yield of single-scattered particles from the first interface.

2.3.6 The final model

We have derived the mathematical formulas as well as experimental factors contributing to the SS model. As a conclusion, the number of detected particles n_i which experienced only one scattering event within the sample with consideration of the angular restriction for previous interfaces equals

$$n_i = n_i' \cdot (1 - W(\alpha, i)); \quad i \geq 2,\, \alpha = 2°, ..., 9°, \tag{2.4}$$

in the full notation:

$$n_i = n_{i-1} \cdot \frac{\sigma_i}{\sigma_{i-1}} \cdot \left(1 - \sum_{i-1} P_{(\alpha)} \cdot (1 - (P_{(2°)} - P_{(\alpha)}))/(i-1)\right); \quad i \geq 2,\, \alpha = 2°, ..., 9°. \tag{2.5}$$

The bracket $(1 - W(\alpha, i))$ takes into account the fact that in hypothetical case of $W(\alpha, i) = 0$, i.e. no scattering under α, the number of detected particles n_i from interface i would be different from the previous interface $i - 1$ only by the term (σ_i/σ_{i-1}).

2.3.7 Double-collision compensation and semi-intuitive essence

The weight function $W(\alpha, i)$ only deals with a case when backscattering under $\theta = 152°$ occurs. From a practical point of view, we have to admit that a particle backscattered from, for example, the second interface under $\theta = 145°$ could be re-routed back to the detector by scattering under 6° from the first interface. We could state a lot of similar DC examples for each interface. These events are of a stochastic nature and cannot be approximated trivially, thus the simulations are implemented. Our approach is just dealing with an ideal case - backscattering under the desired angle θ and scattering under fixed angles for each interface. These effects are to some extent compensated by the procedure of finding the starting point - we take into an account contribution of these events to the resulting yield. As we discuss in section 2.6, correct estimation of mentioned non-ideal contributing DC events undeniably plays a crucial role in general single-scattering evaluation.

Taking all the arguments into account, the model is in its essence *semi-intuitive* - driving procedure deals with a part of collisions that represent the average of possible scattering events and hence might contain the mathematical inequities. Yet, the practical results are surprisingly satisfactory, as we show in the following sections.

2.4 Application of the model

Fortis fortuna adiuvat.
- Latin proverb

We now demonstrate the application of our model on the previously shown spectrum of pure 3.3 nm thick Mo sample. The result is shown in Figure 2.9.

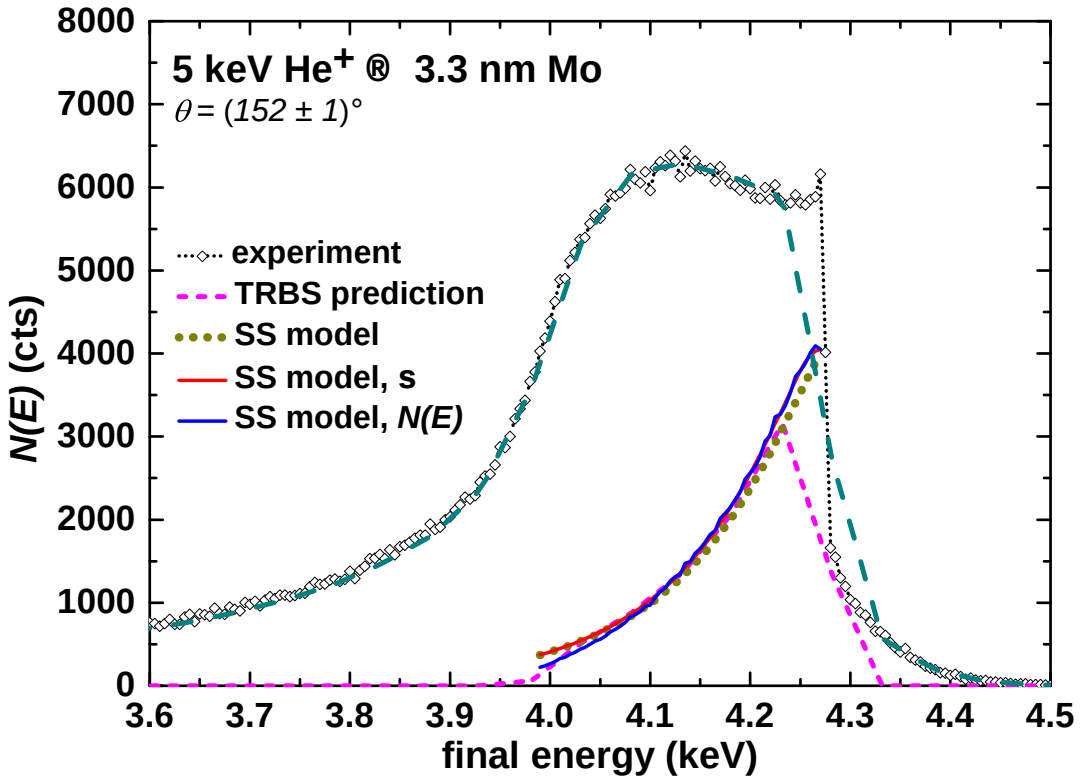

Figure 2.9: Application of the SS model on the TRBS experiment. Single-scattering curve (dotted dark yellow line) was computed using the Equation 2.5. Curves denoted as SS model, σ (solid red line) and SS model, *N(E)* (solid blue line) were computed similarly, but with respect to the number of bins in the TRBS Mo peak. For the latter curve, the ratio of neighbouring yields instead of the ratio of neighbouring cross-sections, as discussed at the end of subsection 2.3.5, was utilized.

The dark yellow dotted line corresponds to the SS model computed with Equation 2.5, i.e. it is directly bound to the actual number of interfaces. The red solid line is, on the contrary, linked to the number of bins - detected final energies - which are present in the FWHM of the peak. For depicted case, the number of bins - energies between $4.27 - 3.99$ keV - equals 57. A practical problem arises: Equation 2.5 is designed to deal with an actual number of interfaces in the sample, which is 11, so up to 10 interfaces to pass for a particle backscattering from the last one. Presented spectrum, however, consists of 57 hypothetical interfaces, i.e. up to 56 to pass after backscattering from the deepest one. In other words, one interface is in the experimental spectrum represented by $56/10 = 5.6$ 'interfaces'. Utilizing our model would lead to extreme, unrealistic attenuation. How do we compensate discussed the undesired phenomenon?

At first, we link P_α to those bins corresponding to the interface: bins from $1-6$ have $P_{(2^\circ)}$, bins from $7-12$ have $P_{(3^\circ)}$ etc.

Secondly, we create an auxiliary vector of layers $norm(i)$ in the following fashion: bins from $1-6$ equals 1, corresponding to the interface 1. For the rest of the bins - $7, 8, 9, ...57$ - each is divided by 5.7 to ensure that for bin 57 we obtain interface 10. Note that we need to obtain the number of interfaces to pass through, not the number of all interfaces, since discussed procedure substitutes the term $(i-1)$ in Equation 2.5 by the term $norm(i)$. Therefore particle scattering from the last interface $i = 11$ has to penetrate through 10 interfaces $11 - 1 = 10$, which is the number given by $norm(57)$.

Finally, we divide $W(\alpha, i)$ by an empirical factor, with no physical meaning, to fit the curve to correct SS curve in the energy range $3.99-4.1$ keV. In our case, a value 25.5 was required.

The described procedure leads to a difference in the shape of obtained curves, the red one is less skewed at the beginning than the dark yellow one. This fact, however, does not influence the result in any significant manner and dealing with this discrepancy requires a suitable programming procedure which has not been orchestrated yet. The blue curve was obtained by the substitution of the cross-section ratio by the ratio of actual yield corresponding to the detected energies, as discussed at the end of subsection 2.3.5. Magenta dashed line is a TRBS prediction of SS yield. Since the program allows to investigate particles collisional distribution only with the binning of 100, as mentioned in section 1.9, we compared the 300 bin experiment with 100 bin spectrum (dark cyan dashed line) by fitting the FWHM of both peaks on the high-energy edge. Another important note concerning TRBS is that the acceptance angle for collisional distribution investigation is 10° without an option to adjust it to a particular experiment. As could be observed, our model in a very good agreement with TRBS prediction. What could also be noted is that the red and the blue solid lines are deviating from each other. Before we discuss the difference between them, we need to clarify one more assumption we made while introducing the model.

In subsection 2.3.2 we admitted that $P_{(\alpha)}$ is increasing with the depth, for presented 9° scattering the difference was 3.1%. We claimed that this fact has no influential effect on our model. The claim is now to be justified, implementing even higher scaling $(\sigma_i/\sigma_1|_{\theta=152})$, which increases for the case of $E = 3.99$ keV by 8.3% with reference to the case of $E = 4.27$ keV. The result is shown in Figure 2.10. No violent discrepancies between the original model (red solid line) and the one corrected by the cross-section scaling (blue dashed line) are observed. As can be seen in the inset the models deviate slightly above 3% for the deepest interface. Henceforth, we assume that using the difference 3.1% instead of used 8.3% would lead to no discrepancy and thus need not to be considered. It is, however, wise to expect that for thicker samples this discrepancy might begin to interfere with the result in a non-negligible manner. Nonetheless, in a classical LEIS experiment, due to its low penetration depth, thin layers are the subject of investigation, hence the approximation of a constant $P_{(\alpha)}$ throughout the sample can be considered as a non-harming presumption. On the other hand, the model is extremely sensitive to the number of interfaces, as demonstrated in the same figure, (b).

The mentioned discrepancy between red and blue solid lines is the different attenuation of these curves starts from the energy around 4.115 keV to the low-energy edge of the peak. The reason is the change of curvature of the experimental peak, as the number

of detected particles $N(E)$ decreases. However, as we are showing in section 2.5, this behaviour of SS model is a common feature of a peak and attempts to compensate it would not provide any more valuable assets to the discussed specifics of the results.

Changes in the SS model for samples of different Mo concentration in their first half will be discussed in the following section.

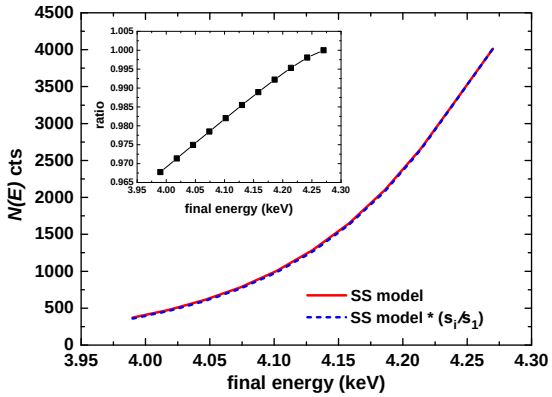

(a) Original model (red solid line) compared to scaling of cross-section (blue dashed line).

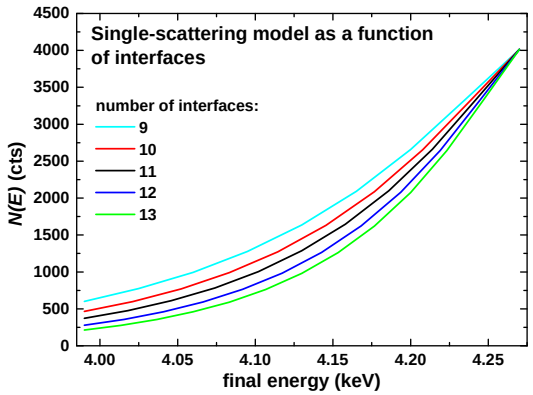

(b) Sensitivity of the model to the number of interfaces

Figure 2.10: Model sensitivity on included probability increase towards the deeper layers (a) and discrepancies between different numbers of interfaces (b).

2.5 Multi-layered samples

All models are wrong, but some are useful.
- George Box

Expanding the possible applicability of the model, we will now discuss the situation in which He projectiles with the same initial energy as in the previous section are probing 3.3 nm thick samples, where the first 1.65 nm contains Mo and silicon - Si - in different mutual concentrations and the second 1.65 nm consists of pure Mo, as shown in Figure 2.11. From now on, we will be denoting the areas with different concentrations as *layers*.

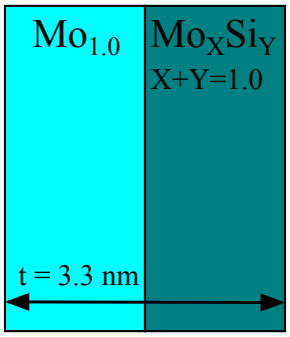

Figure 2.11: Sample with a thickness of 3.3 nm divided into two identically thick areas with the upper one containing Mo and Si in different concentration and the deeper one consisting of pure Mo.

The density of the compound layer was assumed as

$$\rho = X \cdot \rho_{\mathrm{Mo}} + Y \cdot \rho_{\mathrm{Si}}. \tag{2.6}$$

The number of interfaces remained 11, implying that we kept the Mo lattice parameter intact. Values of S_{e} in TRBS were also kept at default, the same as for the pure Mo sample. We executed experiments for the mutual concentrations of Mo/Si (80/20)%, (60/40)%, (50/50)% and (40/60)% with corresponding densities for the compound layers. Cut-off angle remained 9°, as it is a product of the kinematic factor exclusively, depending only on the masses of the projectile-target pair and the scattering angle, as discussed previously in section 1.1. Experimental spectra are shown in Figure 2.12. It could be seen that decreasing concentration of Mo leads to lowering of the high-energy edge of the peak. Low-energy edge is influenced less significantly. In Figure 2.13 correct SS model (dark yellow dotted line) with SS model, σ (red solid line) and SS model, *N(E)*(blue solid line) models are shown. Colours of the lines correspond to those in Figure 2.9. As the abundance of Mo decreases in the first layer, more visible discrepancies in the yield between these curves $n(N(E))/n(\sigma)$ are observed. From the described difference, an idea of extraction of possible information about Mo concentration in the upper layer was born. Comparison of $n(N)/n(\sigma)$ in Figure 2.14 shows an interesting scaling.

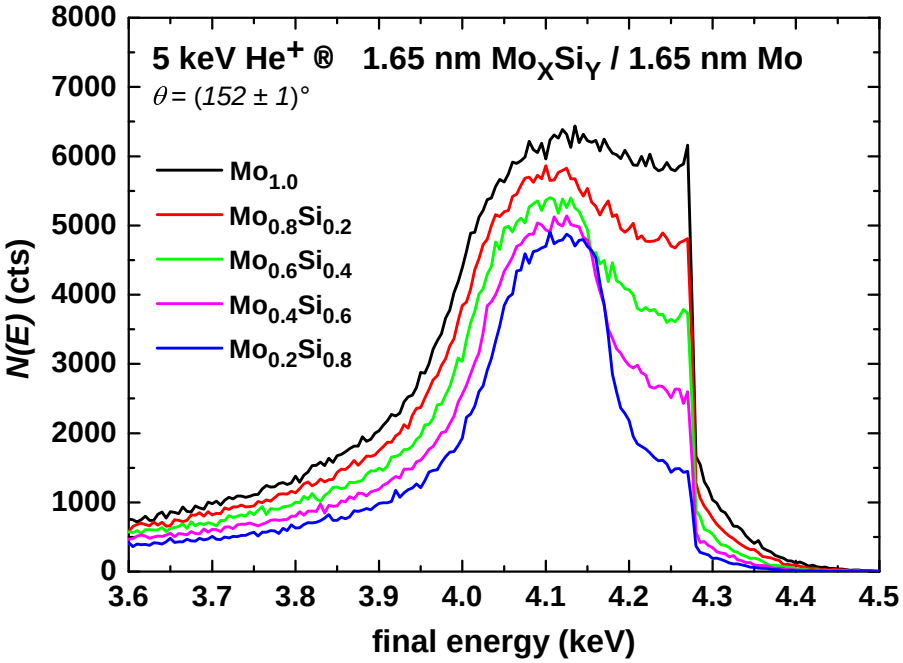

Figure 2.12: TRBS experiments for various MoSi concentrations in the first half of the sample.

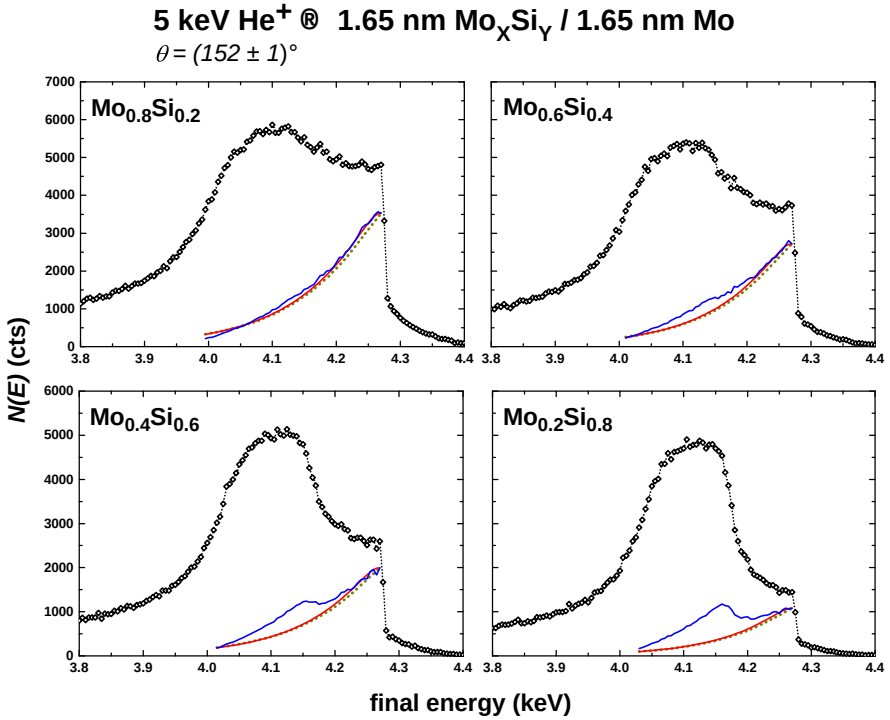

Figure 2.13: TRBS experiments with corresponding SS model for various concentration of Mo and Si in the first half of the sample.

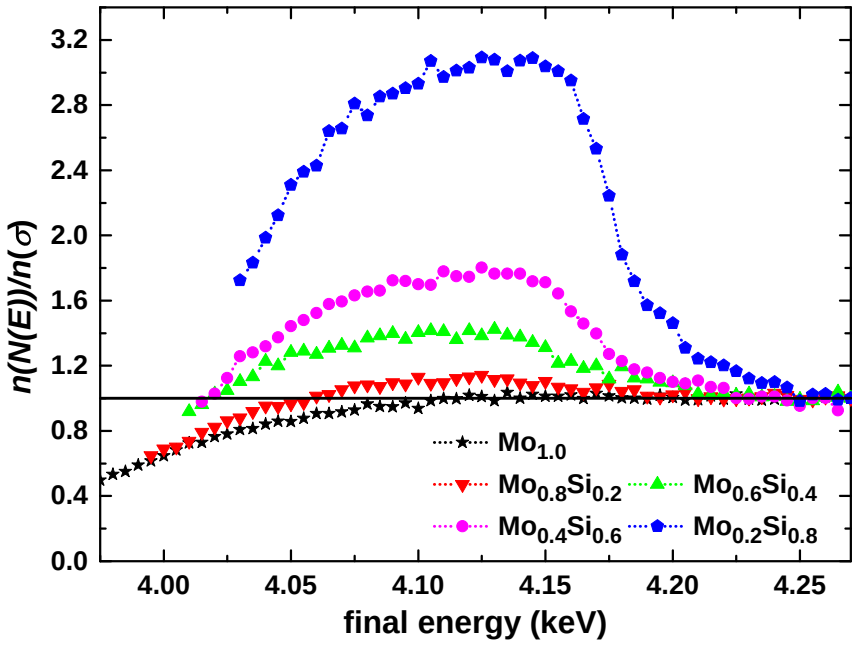

Figure 2.14: Ratios of experimental and cross-section curves for different Mo concentrations. Black dotted line with asterisks corresponds to the sample of pure Mo. Changes in Mo concentrations do not lead to linear changes between respected ratios.

It is clear that experimental curves are deviating from the cross-section ones to the higher yields at the abrupt changes of Mo ratio in the samples. The changes are being shifted to the right for decreasing concentrations since electronic stopping values are lower for layers where Mo atoms are less abundant. Discussed changes are a result of the default characteristic of the model, which assumes a uniform density of the layer when calculating only with the rate of cross-sections. More significant differences in Mo concentrations - spectral shape - naturally lead to more visible differences between SS models. The curves are decreasing towards the low-energy edge due to peak curvature, similarly as in the pure Mo case. Depicted ratios are showing an interesting trend: linear change in Mo concentration does not lead to a linear change in the height of the 'ratio peak'. The scaling is stated in Table 2.2.

consistence of the first layer	maximum value
$Mo_{1.0}$	1.036
$Mo_{0.8}Si_{0.2}$	1.143
$Mo_{0.6}Si_{0.4}$	1.409
$Mo_{0.4}Si_{0.6}$	1.802
$Mo_{0.2}Si_{0.8}$	3.092

Table 2.2: Consistence of the mixed MoSi layer and its corresponding maximum of ratio.

Before we continue with further analysis, it is important to mention a discrepancy between S_e used by TRBS and more updated values available in SRIM 2013 [15] database. The latter is almost two times higher than the TRBS one. Therefore, this correction should be applied to our TRBS experiment. Albeit that is true, we should expect that S_e for upper MoSi layer is also incorrect in TRBS. Moreover, SRIM encourages the user to adjust electronic stopping for compounds as well, so we cannot obtain any value without

comparison with the real experiment. Correcting the bottom layer is therefore redundant for the presented work. In the following text, we assume that the correct values of stopping power in both layers would lead to similar observations.

As shown in the table, the scaling of maximum value does not appear to enable direct entanglement with the Mo concentration in the layers. A naïve expectation would be that the differences in the ratio peaks would be even or at least their scaling trend would be linear. In contrary, tabulated values are showing rather haphazard behaviour.
Compromising effects could possibly include:

1. the incorrect density of the compound layer in the input of TRBS;

2. MS and DC events - they might contribute to a different extent for different samples, especially at the interface between the layers;

3. the model is designated to deal with the sample of a known thickness only, without any further specifications about the different densities or a position of the interface in the sample.

Henceforth, in the present state, we are left with the conclusion that the ratios are more complex and the required disentanglement of practical information is not of a straightforward nature.

Before the end of the section, we will mention a possible density correction to the model, despite the fact we claimed it should not be utilized. According to Figure 2.15, the shape of TRBS prediction is met more precisely for introduced density correction between the layers. The correction is utilized rather counter-intuitively: we multiply $W(\alpha, i)$ by $\rho/\rho_{\mathrm{Mo}} = 0.696$ from sixth to the tenth interface, i.e. it seems as if in the layer of higher abundance of Mo atoms we assume the lesser probability of scattering events than in the first compound layer. The fact is that the model uses only the number of interfaces, without any assumption of the density of scattering centres. Multiplying the weight function thus compensate for the fact that there are more backscattering events occurring in the second layer, rather than lowering possible scattering effect during projectile's propagation to the detector. Even though the approach of the correction might seem to be oversimplified, from a practical point of view, there was no other way of applying the correction of this kind - multiplying any other term contributing to Equation 2.5 would lead to an unrealistic increase of the yield. Despite the better agreement with TRBS prediction, as we have already mentioned in the third paragraph of the compromising effects, for a sample of an unknown thickness of layers with different densities, discussed correction is redundant. Our goal was to show that the model is, to some extent, able to include and find a satisfactory agreement with TRBS when investigating multi-layered samples.
Up until now, we have applied our model on different samples with the same initial energy of He projectiles under the same scattering angle. The question of possible applicability for different experimental set-ups will be discussed in the following section.

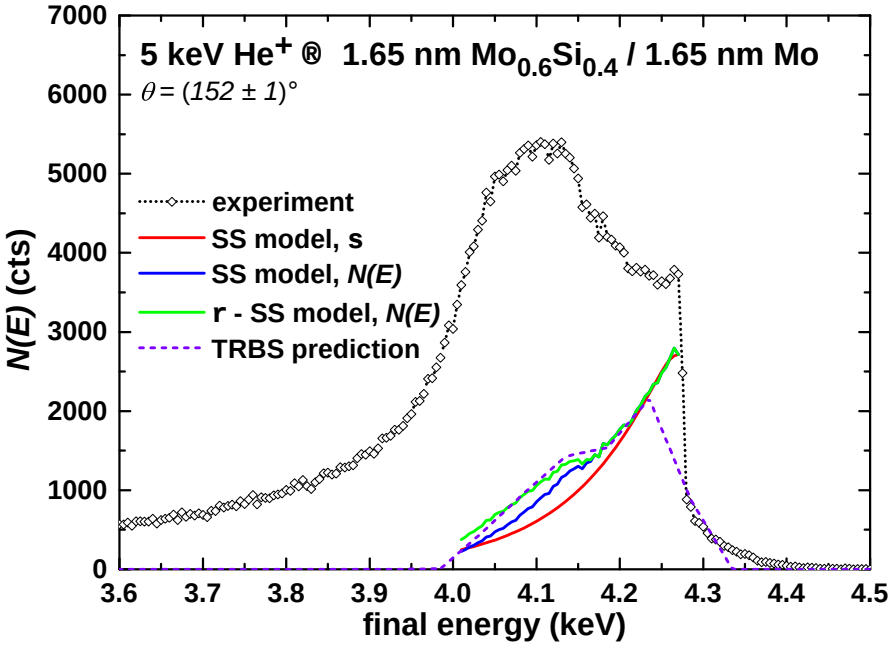

Figure 2.15: Application of a density correction (green solid line) to the SS model, *N(E)*. As an outcome, the shape of TRBS prediction (violet dashed line) is reproduced more accurately than for the uncorrected SS model, *N(E)* (blue solid line). For the comparison, SS model, σ (red solid line) is depicted as well.

2.6 Application on different experiments

Doubt is an uncomfortable condition, but certainty is a ridiculous one.

- Voltaire

To test the reliability of the model is to apply it to the spectra which are examples of a higher energy regime than the one utilized in LEIS. The aim of the section is to demonstrate that the model appears to be applicable to any energy regime, with certain presumptions taken into consideration. Also, only He projectiles are included. For SS model computation Equation 2.5 is used, hence we omitted a computation with the actual number of bins in the experimental peak in this section.

The first experiment was conducted for 30 keV He^+ projectiles impinging on 13.2 nm thick hafnium nitride - HfN - layer atop of a carbon - C - substrate which were subsequently detected under the detector angle $\theta = (135 \pm 2)°$. The lattice parameter of Hf was established at $p = 3.19$Å [18], which corresponds to the shorter distance in its hcp crystal structure. Hence, 41 Hf interfaces were used for the computation. Cut-off angle 12° was opted for, and $\sigma_{1°}$ was chosen as a reference. Calculated probabilities are stated in Table 2.3. The choice of the experimental conditions was not random - the author of the work was confronted with the investigation of different energy spectra of these samples during his Erasmus stay in Swedish Uppsala, hereby they became a foundation for his first steps with TRBS software. Therefore, with a touch of nostalgia, one of the spectra is mentioned in this work.

$interface/\alpha$	$P_{(\alpha)}$
$1/2°$	0.1633
$2/3°$	0.0554
$3/4°$	0.0254
$4/5°$	0.0138
$5/6°$	0.0083
$6/7°$	0.0054
$7/8°$	0.0037
$8/9°$	0.0026
$9/10°$	0.0019
$10/11°$	0.0015
$(11-40)/12°$	0.0011

Table 2.3: Scattering probabilities for HfN.

Direct application of our model immediately shown a feature we did not originally consider: weight function was orchestrated in a fashion that for the case of the second interface it cuts $(P_{(2°)} \cdot 100)\%$ particles from those backscattered from the first interface. According toTable 2.3, this corresponds to 16.33%. The total yield is, however, slightly increased by (σ_i/σ_{i-1}) ratio. Without any further inputs, the SS model for the presented case is shown in Figure 2.16 as a dark yellow solid line.

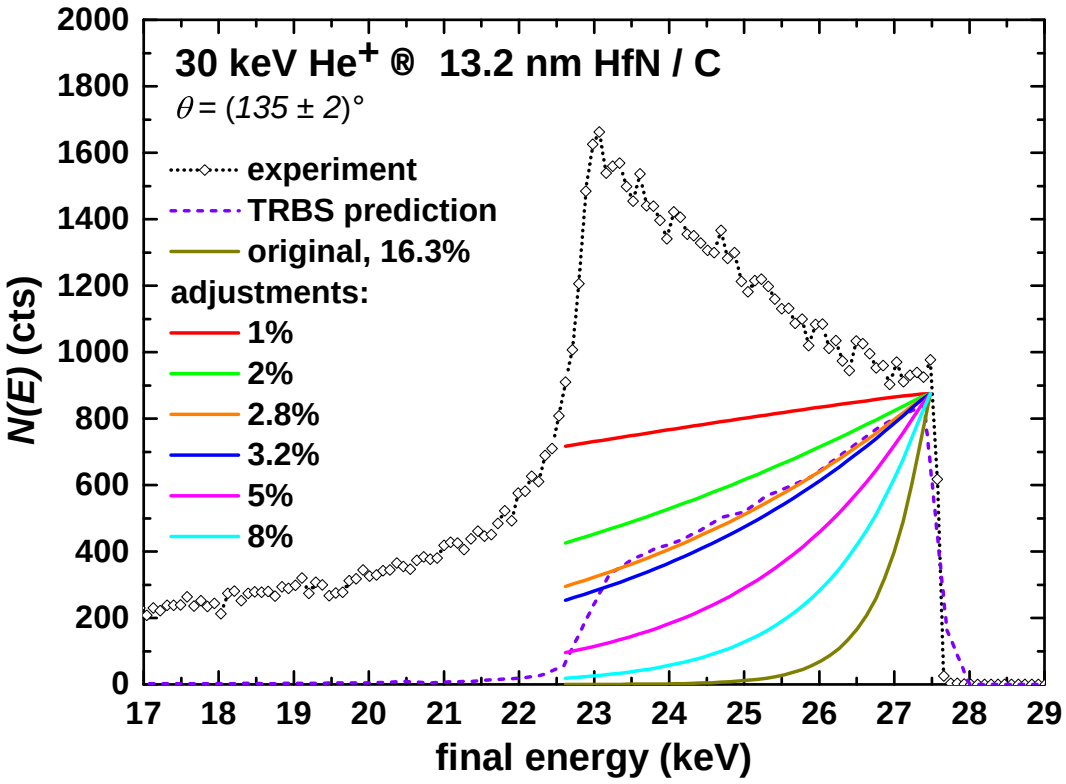

Figure 2.16: Applying the SS model on a spectrum of 30 keV He backscattering from the HfN layer under backscattering angle $(135 \pm 2)°$. The closest fit to TRBS prediction (violet dashed line) was found for 2.8% strictness of the model (orange solid line). For general overview, the sensitivity of the SS model to different adjustments is shown as well.

Clearly, our model is violently deviating from the TRBS prediction. Note that there is no DC contribution to the spectral shape of the peak. Therefore, the condition to cut 16.33% particles from the second interface is too strict - there is no reason to expect their contribution in any drastic manner. Nevertheless, we need to compensate for this fact in the model. Strictness of the second interface, and all $P_{(\alpha)}$ as well, was adjusted to different extent and the results are shown in Figure 2.16. It could be observed that the model is extremely sensitive to presented corrections. The choice of starting point might seem rather suspicious, as it does not begin in the experimental yield but rather slightly below. We will discuss this phenomenon in greater detail in the next example.
Changing the strictness of the second interface from 16.33% to 2.8% (orange solid line) leads to a very good agreement with TRBS prediction. We therefore divided the scattering probabilities by 5.9. Obtaining the introduced number is, unfortunately, practically impossible from the presented spectrum - there is no 'crutch' of how to even roughly approximate DC contributions. However, an interesting connection between Hf and previously discussed Mo cases exists: it is intuitive that cross-sections for respected cases differ due to different scattering angles, primary energy regimes and projectile-target combination. After their comparison, a σ-ratio

$$\frac{\sigma_{\mathrm{Mo}(\theta=152^{\circ};E=5\,\mathrm{keV})}}{\sigma_{\mathrm{Hf}(\theta=135^{\circ};E=30\,\mathrm{keV})}} = 4.97 \tag{2.7}$$

resulted in the number by which $P_{(2^{\circ})}$ was divided and 3.28% strictness was obtained. This result (blue solid line) slightly underestimates TRBS spectral shape. On the other hand, the end of simulation prediction, around 22.5 keV, does not drop to zero despite the HfN layer ends. Subtracting the bump would lead to very good agreement between the prediction and 3.28% strictness of the model.
Acceptance angle of the detector for presented HfN case is 2°. When introducing the model, we stated that chosen reference $\sigma_{1^{\circ}}$ was opted for due to acceptance angle of 1°. We did not compensate this fact in any manner for the investigation, yet a good agreement between prediction and our model was obtained. Henceforth, a conclusion could be made that the detector angular interval need not to be taken into consideration and reference of cross-section for 1° can be established as an universal parameter of the model.

At this point, a note about the application of introduced phenomenon in our previous data ought to be discussed. According to Figure 2.9 the model is in a good agreement with the TRBS prediction. At the present state of the work, the achieved result should be denoted as coincidental - it simply fits the simulation without any violent deviations. Nevertheless, the strictness of the second layer should be discussed - why does it correspond so well with a TRBS spectral shape?

We are now entering a part of the work which relies on the arguments of questionable nature. Yet, it is unavoidable to mention this phenomenon due to its undeniably practical usefulness, if extracted with reasonable precision. The Mo peak from Figure 2.9 will now be subjected to further analysis. Our ideas will revolve around Figure 2.17.

The starting point (red point), i.e. the first interface, is evaluated the same as at the beginning of subsection 2.3.5. It is important to note that the DC contribution (cyan point) is obtained from the experimental spectrum. Blue and cyan point are two bins apart. Having this fact in mind, we got a yellow point which is an outcome of a linear approximation of DC events contribution at the energy level of the second interface.

The corresponding yield from the experiment is marked by a magenta point. However, it was lowered to the same level as the blue one for the plateau trend does not seem to be applicable for the beginning of the experimental peak, which exhibits horizontal behaviour, as depicted in the figure.

According to linear DC approximation, the number of particles after backscattering should be equal to 3338 (the violet point) rather than 3333 obtained by application of the original model. The ratio between red and violet point is 0.8318, i.e. contribution of the second interface ought to be by 16.82% less than from the first interface. The model, however, according to Table 2.1, predicts 16.96% decrease in yield due to the term of cross-section ratio contributing to the result as well: $(\sigma_i/\sigma_{i-1}) \cdot (1 - P_{(2^\circ)}) = 1.009 \cdot 0.8230 = 0.8304$. There are two possible ways of how to utilize obtained correction:

1. to multiply the resulting yield n_i by the ratio between DC and original model prediction 0.8318/0.8304 and obtain term $n_{i,DC} = n_i \cdot 1.0017$ (red solid line);

2. to divide $P_{(\alpha)}$ by the number obtained from equation $(1-P_{(\alpha)}/x)(\sigma_i/\sigma_{i-1}) = 0.8318$, which results in $x = 1.0079$ (royal dashed line).

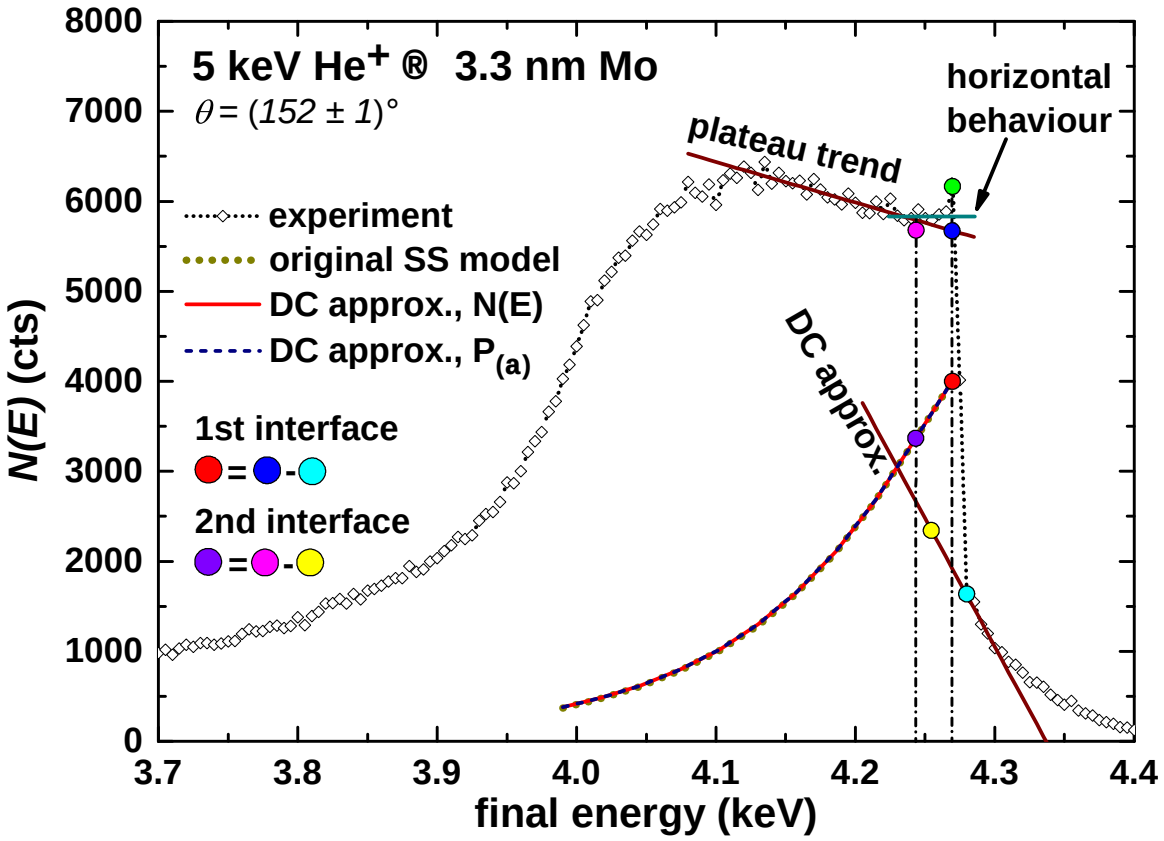

Figure 2.17: Application of the DC correction to $N(E)$ from respected interface (red solid line) and to $P_{(\alpha)}$ (dashed royal line). For depicted case, the obtained curves practically do not differ from the original SS model (dotted dark yellow line). Procedure to establish the DC contribution for the second layer is depicted as well.

To further understand a seemingly coincidental relation between models for two discussed spectra, an experiment for 15 keV He projectiles backscattering under $(145 \pm 1)^\circ$

from 7.5 nm thick golden - Au - layer was conducted. We opted for a cut-off angle of 13°. The number of interfaces was estimated at 19 [18]. Scattering probabilities were evaluated by the unchanged procedure and are stated in Table 2.4. The result is shown in Figure 2.18.

$interface/\alpha$	$P_{(\alpha)}$
1/2°	0.1747
2/3°	0.0598
3/4°	0.0273
4/5°	0.0146
5/6°	0.0087
6/7°	0.0056
7/8°	0.0038
8/9°	0.0027
9/10°	0.0020
10/11°	0.0015
11/12°	0.0012
(12 – 18)/13°	0.0009

Table 2.4: Probabilities for Au.

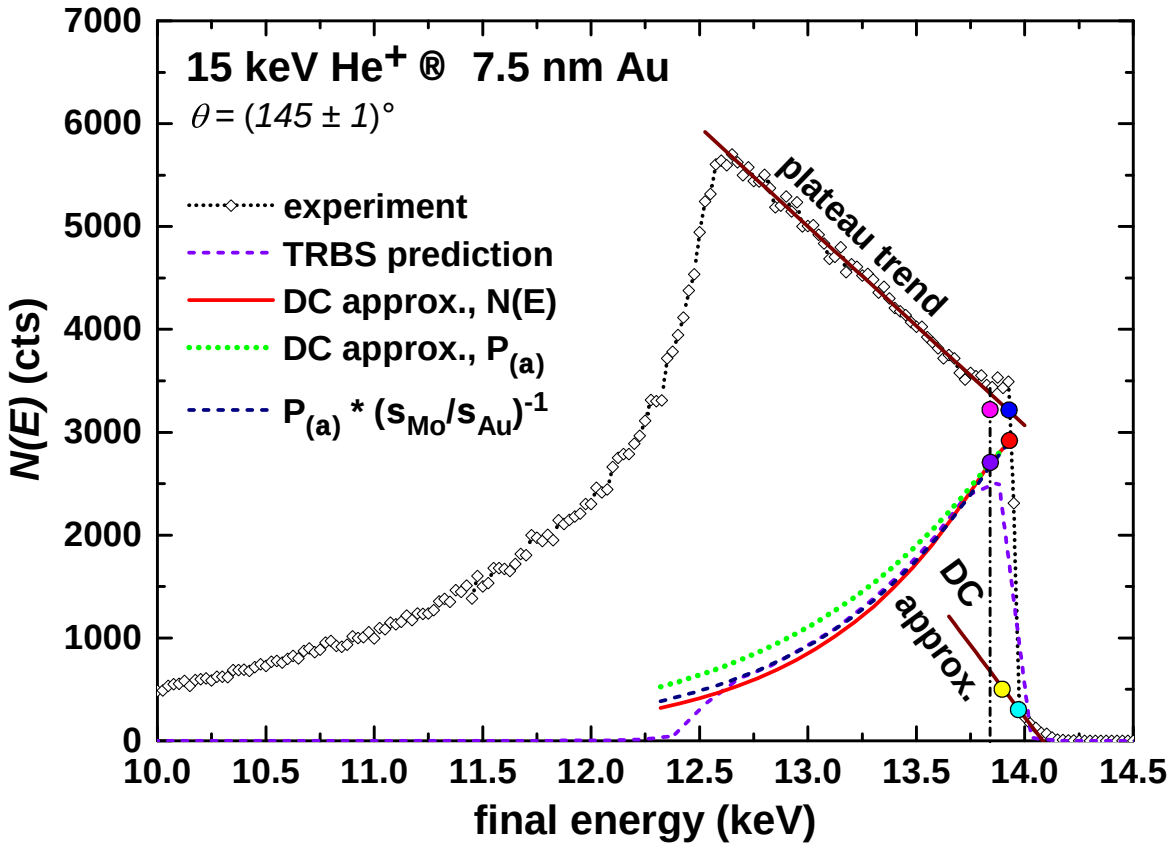

Figure 2.18: Application of both DC correction and σ-ratios

Establishing the starting point was the same as for the Mo case - despite there is no visible surface peak, the same as for the HfN sample, starting trend of experimental peak

differs from general horizontal plateau behaviour, similarly to Figure 2.17. We, therefore, approximated plateau trend by linear fit and from its intersection with the hight energy edge of the peak we subtracted additional surface effects ending up with the blue point. Subsequently, we lowered the starting point by the contribution of DC events and the starting (red) point was obtained. The approach of linear fitting of DC events for the second interface resulted in a yellow point. The corresponding yield from the experiment is marked by a magenta point. This was lowered to the same level as the blue one because of the same reason as in the previous spectrum.

Subtraction of the yellow point from the magenta one demands the strictness of the second interface 7.2% instead of presumed 16.35%. Hence we need to divide $P_{(2^\circ)}$ by 2.117 or to multiply the resulting yield by 1.109. Utilizing the σ-ratio

$$\frac{\sigma_{\mathrm{Mo}(\theta=152^\circ;E=5\,\mathrm{keV})}}{\sigma_{\mathrm{Au}(\theta=145^\circ;E=15\,\mathrm{keV})}} = 1.83 \tag{2.8}$$

results in the value different by 13.6% from DC fit evaluation for scattering probability. As shown in the Figure 2.18, applying DC correction on the yield (solid red line) slightly underestimates TRBS predictions (dashed violet line), whereas DC correction for $P_{(\alpha)}$ (green dotted line) visibly overestimates the prediction. Surprisingly, σ-ratio for respected experimental cases (dashed royal line) reproduces TRBS spectral shape the most accurately. The presented example demonstrates the issue with DC approximation - since the solid red and green dotted lines are deviating from each other in quite a significant way, we conclude that the approximation was too imprecise. Note that in the previous case for Mo, these two practically coincides.

Determination of DC events contribution to the height of the spectrum at the backscattering energy of the second interface does not stand on a solid ground, since it requires a proper knowledge of which part of the DC events at the surface energy should be taken into consideration for the linear fit and if the fit can be linear in the first place. We merely show it as an interesting feature of how experimental spectra could be moulded.

At the presented state of work, analysis of different experimental conditions might be achievable by establishing a precedent: assuming that SS model for Mo peak is correct, then, *stare decisis*, after the utilization of σ-ratio the model for other experiments can be derived.

2.7 The real experiment

A journey of a thousand miles begins with a single step.
- Laozi

We are in the endgame of our work, which is dedicated to application of the model to the real experiment. The only parameter known about the obtained spectrum is its thickness 3.3 nm, hence we still assume 11 interfaces, and different concentration of Mo in its respected areas, whose thickness is unknown. The result of our attempt is shown in Figure 2.19.

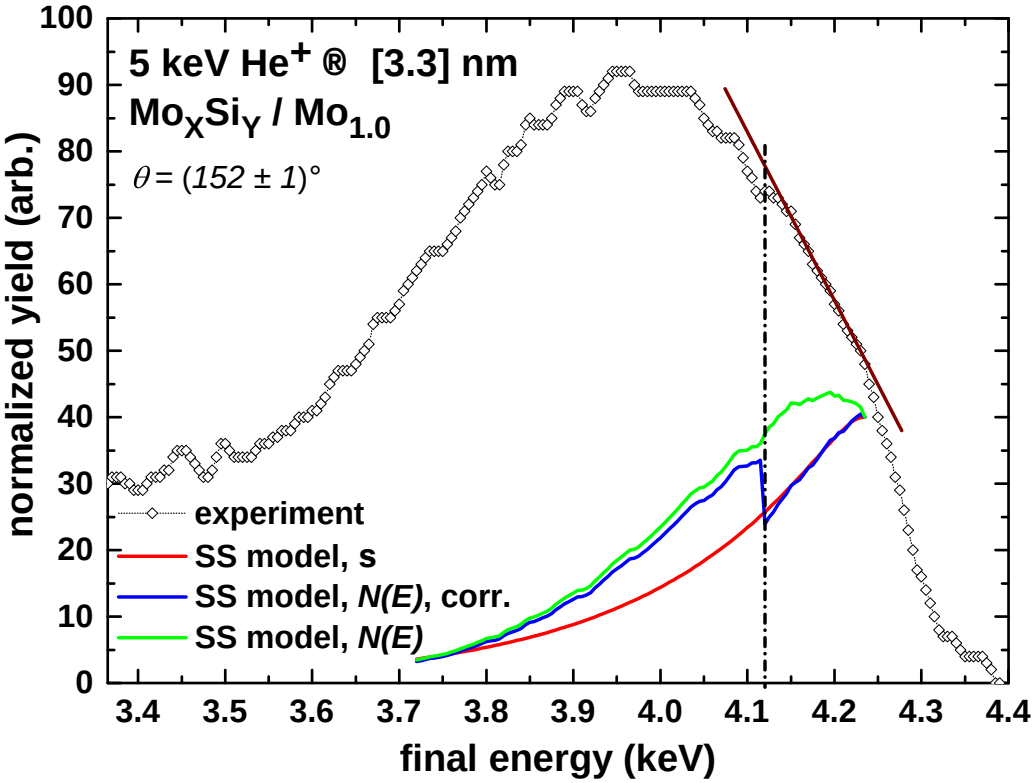

Figure 2.19: Application of the SS model to the real experiment.

Because of detector resolution and other compromising effects present in real experiments, we observe almost a smooth peak, not even slightly resembling the shape of TRBS peaks investigated in section 2.5. Experimental (green solid line) model is rising from the high-energy edge, despite the fact it should be corresponding to the SS model computed via cross-sections (red solid line) at least for a part close to the surface. Boldly, we assumed the linear behaviour of the 'plateau' from the point where the contribution of particles backscattered from the surface could be expected. Approximately at final energy 4.11 keV the shape of peak starts to behave differently. This was assigned to point where the change in Mo concentration within the sample takes place, as depicted in Figure 2.20.

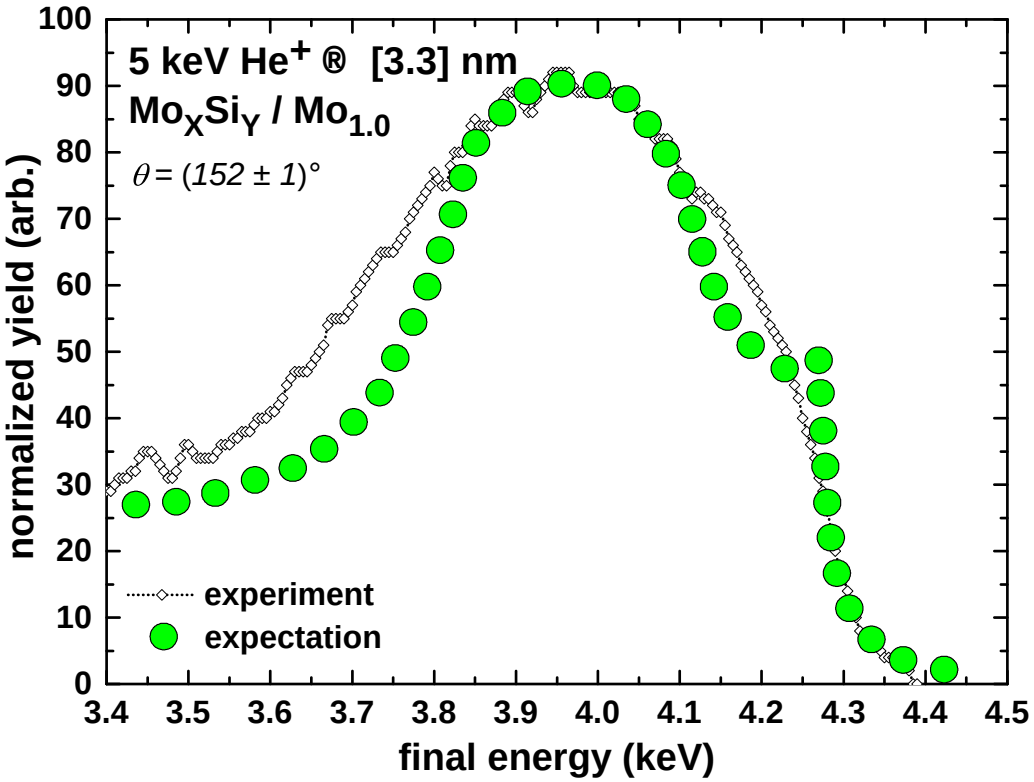

Figure 2.20: Expectation of the spectral shape (green points) without the undesired, yet unavoidable experimental compromising effects.

With the optimistic presumption, we forcefully lowered the experimental model to match the cross-section model for the entire linear behaviour of the peak. Lowering was conducted by simple subtraction of empirical value 1.2 and we recorded the difference between the uncorrected ratio of neighbouring yields and the corrected ones

$$(N_i/N_{i-1}) - (N_i/(N_{i-1} - 1.2)). \tag{2.9}$$

Next, we rose up the experimental spectrum by simply adding the sum of differences introduced in Equation 2.9 at the point of expected change in Mo concentration. The discrepancy between somewhat corrected experimental model (blue solid line) and those obtained from TRBS is its abrupt change of the shape - attempting to describe a procedure to smooth the transition would be, without doubt, completely random. Not to conceal something, the entire investigation of the experimental peak is suspicious, if for nothing than certainly due to the fact that it was not tested on the clean surface of Mo for a reference. The method of how to avoid investigation of the experiment is to use TRBS and apply the model on such spectrum. A disadvantage of the described approach is that correct stopping power and screening model ought to be known for both layers with different Mo concentrations. As an outcome, a future possibility of successful depth profiling from the experiments remains uncertain.

The entire section is a proof that the model is in its beginning and for its future applicability, extensive work has to be done.

Conclusion

In presented work, we introduced the new model for evaluation of the contribution of single-scattered projectiles to the entire experimental peak. The investigation of Mo samples probed with He projectiles brought satisfactory results - our model agreed with TRBS prediction. Different energy regimes and experimental set-ups - HfN and Au samples investigated by the same projectiles under backscattering angles $(135 \pm 2)^\circ$ and $(145 \pm 1)^\circ$, respectively - introduced a peculiar entanglement with Mo experiments - comparison of cross-sections, at respected primary energies and for respected detector angles, enables to smoothly apply the model from one spectrum to another, in case that the first one was established as correctly evaluated. Approximative approach concerning double-collisions opens no less peculiar possibilities of spectral evaluation and possible future investigation. The real experiment, however, reminds an uncomfortable truth - compromising effects almost completely prevent the model to be straightforwardly applied. Despite these obstacles, we at least managed to outline a possible course of depth profiling that could be disentangled from experiments.

Bibliography

[1] ALFORD, T. L., FELDMAN, L.C., MAYER, J. W. *Fundamentals of Nanoscale Film Analysis*. Springer US, 2007. ISBN: 978-0-387-29260-1.

[2] DRAXLER, M., MARKIN, S. N., ERMOLOV et al. *ACOLISSA: a powerful set-up for ion beam analysis of surfaces and multilayer structures*. In: *Vacuum*. 2004, **73**(1), 39–45. DOI :10.1016/j.vacuum.2003.12.041.

[3] RABALAIS, J. W. *Principles and Applications of Ion Scattering Spectrometry: Surface Chemical and Structural Analysis*. 2002. ISBN: 978-0-471-20277-6.

[4] CUSHMAN, C.V, BRUNER, P., ZAKEL, J. et al. *Low energy ion scattering (LEIS). A practical introduction to its theory, instrumentation, and applications*. In: *Analytical Methods*. 2016, **8**(11), 3419-3439. DOI: 10.1039/C6AY00765A.

[5] BULGARADYAN, D., SINELNIKOV, D., KURNAEV, V. et al. *Application of keV-energy proton scattering for thin film analysis*. In: *Nuclear Instruments and Methods in Physics Research Section B: Beam Interactions with Materials and Atom*. 2019, **438**, 54-57. DOI:10.1016/j.nimb.2018.10.043.

[6] CHENAKIN, S.P., MARKIN, S.N., STEINBAUER E. *Electronic stopping of hydrogen ions deduced from TOF-LEIS spectra*. In: *Nuclear Instruments and Methods in Physics Research Section B: Beam Interactions with Materials and Atoms*. **249** (1-2), 2006, 58-61. DOI: 10.1016/j.nimb.2006.03.023.

[7] CUSHMAN, C. V., BRUNER, P., ZAKEL, J. *Low energy ion scattering (LEIS). A practical introduction to its theory, instrumentation, and applications*. In: *Analytical Methods*. 2016, **8** (17), 3419-3439. DOI: 10.1039/C6AY00765A.

[8] BRONGERSMA, H. H., DRAXLER, M., DE RIDDER, M., BAUER, P. *Surface composition analysis by low-energy ion scattering*. In: *Surface Science Reports*. 2007, **62** (3), 63-109. DOI: 10.1016/j.surfrep.2006.12.002.

[9] BRONGERSMA, H. H. *Characterization of Materials*. J. Wiley & Sons, 2012. 2. edition. DOI: 10.1002/0471266965.

[10] CHENAKIN, S.P., KOLAROVA, R., MARKIN, S.N. et al. *Influence of screening and electronic stopping on LEIS spectra*. In: *Nuclear Instruments and Methods in Physics Research Section B: Beam Interactions with Materials and Atoms*. 2007, **258** (1), 32-35. DOI: 10.1016/j.nimb.2006.12.173.

[11] DUDA, R. *Analýza nanostruktur metodou TOF-LEIS*. Brno: Vysoké učení technické v Brně, Fakulta strojního inženýrství, 2015. 91s. Vedoucí dizertační práce prof. RNDr. Petr Dub, CSc.

[12] BIERSACK, J.P., STEINBAUER, E., BAUER P. *A particularly fast TRIM version for ion backscattering and high energy ion implantation*. In: *Nuclear Instruments and Methods in Physics Research Section B: Beam Interactions with Materials and Atoms*. 1991, **61** (1), 77-82. DOI: 10.1016/0168-583X(91)95564-T.

[13] MOLIÈRE, G. *Theorie der Streuung schneller geladener Teilchen II Mehrfach- und Vielfachstreuung*. In: *Zeitschrift für Naturforschung*. **3a**, 1948, 78-97.

[14] ZIEGLER, J.F., BIERSACK, J.P., LITTMARK, U. *The Stopping and Range of Ions in Solids*. **1**, Pergamon, New York, 1985.

[15] ZIEGLER, J.F. *The Stopping and Range of Ions in Matter* [cited 10.5.2019]. On-line: `http://www.srim.org`.

[16] SCHMIDT, M. *LEIS Energy Calculator* [cited 10.5.2019]. On-line: `https://www.iap.tuwien.ac.at/www/surface/leis`.

[17] DRAXLER, M., BEIKLER, R., TAGLAUER E. et. al. *Explanation of the surface peak in charge integrated LEIS spectra*. In: *Nuclear Instruments and Methods in Physics Research Section B: Beam Interactions with Materials and Atoms*. 2003, **203**, 218-224. DOI: 10.1016/S0168-583X(02)02220-6.

[18] *WebElements* [cited 7.5.2019]. On-line: `https://www.webelements.com`.